EarthArXiv Coversheet

Authors

Evgenii Salganik[1,2*], Benjamin A. Lange[2,3], Polona Itkin[4], Dmitry Divine[2], Christian Katlein[5], Marcel Nicolaus[5], Mario Hoppmann[5], Niklas Neckel[5], Robert Ricker[6,5], Knut V. Høyland[1], Mats A. Granskog[2]

Affiliations

[1] Norwegian University of Science and Technology, Trondheim, Norway
[2] Norwegian Polar Institute, Fram Centre, Tromsø, Norway
[3] Norwegian Geotechnical Institute, Oslo, Norway
[4] UiT - The Arctic University of Norway, Tromsø, Norway
[5] Alfred-Wegener-Institut Helmholtz-Zentrum für Polar- und Meeresforschung, Bremerhaven, Germany
[6] NORCE Norwegian Research Centre, Tromsø, Norway

Emails

[*] evgenii.salganik@proton.me

Peer-review statement

This manuscript is in accepted at Elementa: Science of the Anthropocene and is not peer-reviewed.

Different mechanisms of Arctic first-year sea-ice ridge consolidation observed during the MOSAiC expedition

Evgenii Salganik[1,2*], Benjamin A. Lange[2,3], Polona Itkin[4], Dmitry Divine[2], Christian Katlein[5], Marcel Nicolaus[5], Mario Hoppmann[5], Niklas Neckel[5], Robert Ricker[6,5], Knut V. Høyland[1], Mats A. Granskog[2]

[1] Norwegian University of Science and Technology, Trondheim, Norway
[2] Norwegian Polar Institute, Fram Centre, Tromsø, Norway
[3] Norwegian Geotechnical Institute, Oslo, Norway
[4] UiT - The Arctic University of Norway, Tromsø, Norway
[5] Alfred-Wegener-Institut Helmholtz-Zentrum für Polar- und Meeresforschung, Bremerhaven, Germany
[6] NORCE Norwegian Research Centre, Tromsø, Norway
[*] evgenii.salganik@proton.me

Abstract

Sea-ice ridges constitute a large fraction of the ice volume in the Arctic Ocean, yet we know little about the evolution of these ice masses. Here we examine the thermal and morphological evolution of an Arctic first-year sea-ice ridge, from its formation to advanced melt. Initially the mean keel depth was 5.6 m and mean sail height was 0.7 m. The initial rubble macroporosity (fraction of seawater filled voids) was estimated at 29% from ice drilling and 43–46% from buoy temperature. From January until mid-April, the ridge consolidated slowly by heat loss to the atmosphere and the total consolidated layer growth during this phase was 0.7 m. From mid-April to mid-June, there was a sudden increase of ridge consolidation rate despite no increase in conductive heat flux. We surmise this change was related to decreased macroporosity due to transport of snow-slush to the ridge keel rubble via adjacent open leads. In this period, the mean thickness of the consolidated layer increased by 2.1 m. At the peak of melt in June–July we suggest that the consolidation was related to the refreezing of surface snow and ice meltwater and of ridge keel meltwater (the latter only about 15% of total consolidation). We used the morphology parameters of the ridge to calculate its hydrostatic equilibrium and obtained a more accurate estimate of the actual consolidation of the keel, correcting from 2.2 m to 2.8 m for average keel consolidation. This approach also allowed us to estimate that the average keel melt of 0.3 m, in June–July, was accompanied by a decrease in ridge draft of 0.9 m. An ice mass balance buoy in the ridge indicated total consolidation of 2.8 m, of which 2.1 m was related to the rapid mode of consolidation from April to June. By mid-June, consolidation resulted in a drastic decrease of the macroporosity of the interior of keel while the flanks had little or no change in macroporosity. These results are important to understanding the role of ridge keels as meltwater sources and sinks and as sanctuary for ice-associated organisms in Arctic pack ice.

Introduction

According to the definition of the World Meteorological Organization (WMO, 2014), an ice ridge is a line or wall of broken ice that is forced up by pressure. Ridges consist of a sail above, and a keel below the water level. The keel initially consists of rubble, randomly packed ice blocks separated by water-filled voids, described by the ridge macroporosity (fraction of rubble consisting of water-filled voids). Due to cooling from the atmosphere, the keels consolidate by freezing of these voids, largely proceeding vertically downwards and forming the consolidated layer (Leppäranta et al., 1995). The fully frozen part of the ridge defined by zero macroporosity is called the consolidated layer, and is usually characterized by temperatures below freezing point of seawater during freezing period. Ice ridges are also key features in climate studies as they constitute a significant and increasing fraction of the ice volume (Rothrock, 2005), typically around 40% (Hansen et al., 2014), and because they melt differently from level ice (Perovich et al., 2003; Amundrud et al., 2004). Moreover, sail heights are key to estimate atmospheric form drag, driving the momentum balance of sea ice (Tsamados et al., 2014). Sea-ice ridges, especially first-year ridges with large macroporosity, are also important for the ice-associated (sympagic) communities, having been identified as potential ecological hotspots and proposed to serve as refugia of ice-associated organisms (Hop and Pavlova, 2008; Lange et al., 2017; Fernández-Méndez et al., 2018). Ridges have been proposed to serve as both a refuge and feeding ground for ice-associated

organisms, with shifting sea-ice habitats and continued disappearance of summer sea ice (Gradinger et al., 2010). While new generations of satellites are able to map the surface topography with unprecedented resolution, capable to detecting the dimensions of ridge sails (Duncan and Farrell, 2022; Ricker et al., 2023), sea-ice ridges remain among the most under-sampled and least studied features of the Arctic sea-ice pack.

Sea-ice ridges can be formed from new, young, first-year, second-year, or multiyear level ice or a combination. Ridges are usually made from relatively thin ice (Tucker et al., 1984), which breaks as the weakest point during deformation events. This understanding was supported by the numerical simulation from Hopkins et al. (1991), showing a strong effect of block thickness on the energy required for ridging. Ridges themselves can also be first-year, second-year, or multiyear depending on how many seasons they survive. First-year ice ridges are usually porous (high macroporosity, meaning high fraction of seawater-filled voids), while multiyear ice ridges can be completely consolidated (Kovacs, 1983). Ridge keels are usually 3–5 times larger than ridge sails (Timco and Burden, 1997). The ridge macroporosity is usually estimated using mechanical ice drilling as the volumetric fraction of voids (Leppäranta and Hakala, 1992). Leppäranta et al. (1995) measured rubble macroporosity of 29–32% for a ridge in the Bothnian Bay (Baltic Sea), Kankaanpää (1997) summarized the results from multiple ridges in the northern Baltic Sea and found a keel macroporosity of about 30–35% on average, Høyland (2007) reported an average rubble macroporosity of 37% for the Barents Sea from 2002–2005, and Kharitonov (2008) found an average keel macroporosity of 12–28% increasing with depth using the thermal drilling method. Leppäranta et al. (1995) investigated a first-year ice ridge in a relatively fresh (2–3 salinity) part of the Baltic Sea from February to April, showing consolidation only during the winter season, with an average keel melt of 0.94 m in spring. Shestov et al. (2018) observed ridge consolidation in spring and melt in summer during the N-ICE2015 expedition (Granskog et al., 2018) in the pack ice north of Svalbard. Consolidated layer thickness increased by 0.5 m over 22 days from May 5 to May 27, while the average ocean heat flux was 4 W m^{-2} (Peterson et al., 2017). During June 10–19, the average ocean heat flux was 63 W m^{-2} (Peterson et al., 2017), and the consolidated layer melted by 1.5 m (Shestov et al., 2018).

Marchenko (2022) examined ridges in the Barents Sea in late April 2017–2019, when all the investigated ridges were already fully consolidated, and formulated a mathematical model of ridge thermodynamics to investigate the influence of keel meltwater on the consolidation of ice rubble. The model assumes that the meltwater contributing to the ridge consolidation only comes from keel melt. That model predicts full consolidation of a ridge with an initial macroporosity of 30%, keel draft of 10 m, an initial consolidated layer of 2.0 m, and ocean heat flux of 20 W m^{-2} after 431 days. The initial ridge observations during the Multidisciplinary drifting Observatory for the Study of Arctic Climate (MOSAiC) expedition indicate that the consolidation of the ridge keels in summer took place much more rapidly, suggesting that there must be other processes that result in more rapid ridge keel rubble consolidation. Lange et al. (in press) showed a substantial contribution (6–11%) of snow to the mass increase of the first-year ice ridges in summer, using analysis of oxygen isotope composition of ice cores from ridges. Their results indicate that snow melt contributes significantly to ridge consolidation in summer.

Here we used rare seasonal in situ data to follow the evolution of a first-year sea-ice ridge from its initial stages to advanced summer melt, using observations carried out during the MOSAiC expedition in the central Arctic. We observed several mechanisms of ridge consolidation, linked to thermodynamic growth in winter, snow-slush transfer to ridge keels during dynamic events and meltwater refreezing during the summer melt period.

Material and methods

Expedition

Nicolaus et al. (2022) present an overview of snow and ice work during the MOSAiC expedition, which took place in 2019–2020 to better understand the coupled Arctic ice, ocean, and atmosphere system and the sea-ice mass and energy budget over a full season. The MOSAiC study area consisted of two regions of cascading size: the smaller approximately 3 km by 4 km large Central Observatory; and the surrounding Distributed Network, which consisted of remote sites in a 40 km radius around the Central

Observatory. In brief, in September 2019, the icebreaker *Polarstern* (Knust, 2017) traveled through the northern Laptev Sea and moored itself inside the ice pack on October 4, 2019. Thereafter the Central Observatory was established, including the installation of ice drilling and coring sites and deployment of ice mass balance buoys (IMBs). This observatory drifted for 10 months across the central Arctic, following the Transpolar Drift, until it reached the ice edge in Fram Strait and broke apart on July 31, 2020. Due to several sea-ice deformation events, the Central Observatory was continuously redesigned, most notably between May and June 2020. Its area decreased to 0.9 km^2 by July 2020. The sea ice of the Central Observatory around *Polarstern* was formed in a polynya north of the New Siberian Islands in December 2018 (Krumpen et al., 2020). The residual ice eventually became SYI, that was formed in December 2018 (or sometime during the following winter) and remained at the start of the drift. It had a modal thickness of 0.37 m on September 25, 2019, based on a series of in situ measurements conducted within the Distributed Network. The Central Observatory reached the marginal ice zone in May–July 2020 (Lei et al., 2022).

The air temperatures remained generally colder than –20°C, broadly defining the winter season from the end of November 2019 to mid-April 2020. In mid-April, a transition to air temperatures warmer than –20°C occurred abruptly, coincident with a southerly warm air intrusion event during April 15–21, 2020, when air temperatures rose to −2°C (Rinke et al., 2021). This abrupt shift signified the spring transition season and the progression towards melt. In late May, as the sea ice reached consistent surface melt, the near-surface air temperature was constrained by the melting snow and ice to a narrow range within a couple of degrees of 0°C (Shupe et al., 2022).

During MOSAiC, the upper ocean was at or colder than the salinity-given freezing temperature until early April (Katlein et al., 2020), and the mixed layer deepened through winter (January to March) likely through sea-ice growth and brine exclusion. However there were also large regional contrasts in the upper ocean salinity during the drift (Rabe et al., 2022). A major change occurred in the turn of March to April, when the mixed layer depth and salinity increased (and temperature decreased). This change was related to the ice floe drifting out of the Transpolar Drift into a regime of Atlantic inflow with higher salinity and less stratification (Rabe et al., 2022).

In the middle of May, the air temperatures reached the freezing point of seawater. Lei et al. (2022) reported ocean heat fluxes of 2.8 ± 1.1 W m^{-2} from December to April, and 10.0 ± 2.6 W m^{-2} by mid-June using SIMBA data, while Salganik et al. (2023) estimated an ocean heat flux increase from 16 to 44 W m^{-2} from July 9 to July 29 using level ice temperatures and bottom melt rates in the Central Observatory. The corresponding bottom melt of FYI was estimated at 0.28 m by July 29.

Ridge drilling

In this study, we focus primarily on the evolution of ‘Alli’s Ridge’. Ice dynamics during December 7–15 led to the formation of a lead 30–100 m wide inside the SYI of the Central Observatory. This lead refroze after mid-December. Alli’s Ridge formed January 4–5, 2020, at the edge of this lead. The southern flank of Alli’s Ridge was built mainly of blocks of the thin lead ice, while the northern flank contained thicker SYI. The ice blocks were 0.2–0.4 m and 0.9–1.0 m thick on the lead and SYI side, respectively. Alli’s Ridge was about 400 m long and connected into a system of ridges in the Central Observatory (**Figure 1**a). At the time of formation, its crest was rising in places about 3 m over the surrounding level ice. During snowfalls in January and February 2020 substantial amounts of snow accumulated on both flanks of the ridge.

We investigated ridge morphology using a 2-inch diameter ice drilling auger (Kovacs Enterprise, USA). Ice drilling was organized along three drilling transects perpendicular to the ridge crest orientation, located 10 m away from each other. Each transect contained 8–11 drilling locations with measurements of ice draft, freeboard, depth of ridge voids, and snow thickness at a horizontal spacing of 2.5 or 5 m (**Figure 1**b). The ridge was visited twice during the winter season (January 17 and February 6) and three times during the summer season (July 9, 15, and 26). During the winter season, 8 vertical drilling profiles were made along the middle transect. During the summer season, 10 vertical drilling profiles were made at the West transect, 10 profiles were made along the middle transect, and 11 profiles were made along the East transect (**Figure S1**). Snow depth along drilling transects was measured manually with a Magnaprobe, an automated snow depth probe (Itkin et al., 2023).

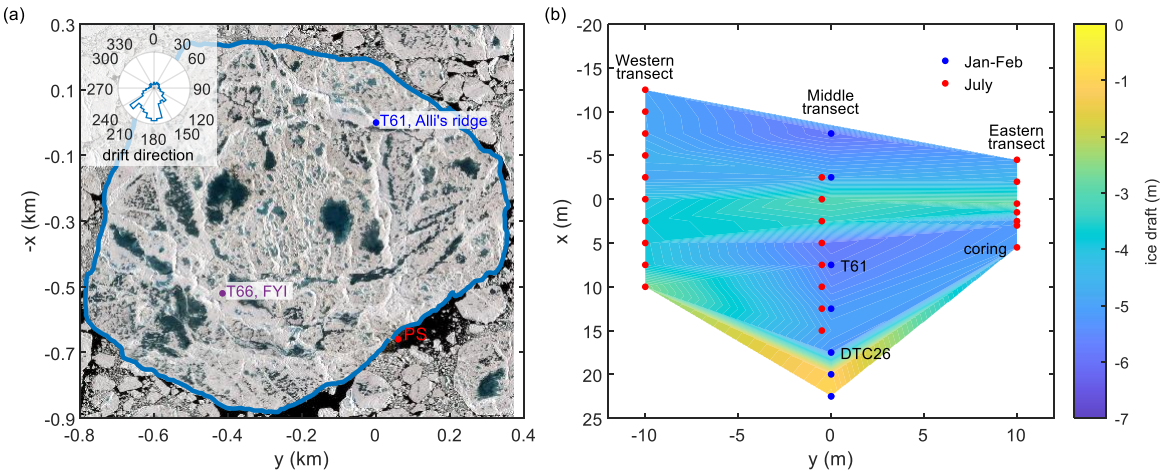

Figure 1. Location of Alli's Ridge, ice mass balance buoys, and drilling transects in MOSAiC Central Observatory. (a) Location of SIMBA ice mass balance buoys 2020T61 (T61, blue dot), 2019T66 (T66, purple dot) and *Polarstern* (PS, red dot) within the Central Observatory outline (blue line). The background is the satellite image of the ice floe on July 1 from Planet Labs. The polar histogram shows the frequency of ice drift direction in relation to the displayed ice floe orientation, with prevailing drift in the South direction (174°; Schmithüsen, 2021). (b) Location of ice drilling at Alli's Ridge with a contour plot of the keel depth (combined drilling data from winter and summer).

Ice mass balance buoys

To study the temporal evolution of thickness and temperature of the ridge and level ice, we used temperature measurements from ice mass balance buoys. Two types of IMBs were used including Snow Ice Mass Balance Array (SIMBA, SAMS Enterprise Ltd, UK) and Digital Thermistor Chain (DTC, Bruncin d.o.o., Croatia). SIMBAs have a chain with sensor spacing of 2 cm, and provide temperature readings every 6 hours with accuracy of 0.1°C. Daily cycles of internal heating of 30 s and 120 s allow to identify the location of snow-ice and ice-water interfaces from SIMBA data with high precision (Jackson et al., 2013). DTC also has a sensor spacing of 2 cm, with the sensors providing in situ temperature and temperature after a cycle of internal heating of 20 s every 6 h with accuracy of 0.25°C. Lei et al. (2022) presented an overview of the SIMBA buoys deployed in the MOSAiC Distributed Network, which included those used in this study for level ice analysis within the MOSAiC Central Observatory: SIMBA 2019T56 (T56) and 2019T62 (T62) installed in level SYI and SIMBA 2019T66 (T66) installed in level FYI in October 2019.

Two IMBs, SIMBA 2020T61 (T61) and DTC 26 (DTC26), were installed on the southern flank of Alli's Ridge in the blocks formed from the refrozen lead (**Figure S2**). On February 5, T61 was installed close to the ridge crest, while DTC26 was installed close to the remaining level ice in the refrozen lead (**Figure 1**). The length of T61 chain was 5.0 m (did not reach ridge keel bottom), while DTC26 was 7.36 m long. At installation, the consolidated layer thickness was 1.0 m and 2.0 m, while keel depth was 6.5 m and 5.2 m at the T61 and DTC26 sites, respectively. Snow depth was 7–8 cm at the T61 site and 1 cm at the DTC26 site at time of deployment.

Sea-ice thermodynamics

The estimate of the conductive heat flux q_c is based on the vertical temperature gradient above the ice-water interface and measurements of ice salinity and density, defining its thermal conductivity. It was calculated from IMB temperature measurements as:

$$q_c = -k_{si}\,\partial T_i/\partial z_i, \quad (1)$$

where k_{si} is the thermal conductivity of sea ice, and $\partial T_i/\partial z_i$ is the vertical temperature gradient.

Latent heat flux of solidification was estimated from the evolution of ice-water interface height as

$$q_l = \rho_{si} L_{si} \eta\, dh_{si}/dt, \quad (2)$$

where ρ_{si} is the density of sea ice, L_{si} is the specific latent heat of sea ice, η is the ridge macroporosity, h_{si} is the sea-ice thickness, and t is the time. The in situ sea-ice density and latent heat were calculated from the relative brine and gas volume of the sea ice, estimated from the measured ice salinity, temperature and density using Cox and Weeks (1983) for cold ice and Leppäranta and Manninen (1988) for ice warmer than −2 °C (**Figure 2**a). Sea-ice thermal conductivity was estimated using Notz (2005). The ridge macroporosity was calculated from the results of ice drilling as the fraction of voids within ridge rubble following Leppäranta and Hakala (1992). The location of the ice-water interface was estimated using in situ temperatures (Salganik et al., 2021) and heating temperatures (Jackson et al., 2013) from IMBs.

The ice cores for temperature, salinity and density measurements were extracted with a 7.25-cm (Mark III) internal diameter ice corer (Kovacs Enterprise, US). Ice temperature was measured in situ using a Testo 720 thermometer in drill holes with a length of half-core-diameter at 10-cm vertical resolution. Ice density was measured using the hydrostatic weighing method (Pustogvar and Kulyakhtin, 2016) with 5 cm vertical resolution from a separate core in the freezer laboratory onboard *Polarstern*. Ice bulk salinity was measured from melted sections of a density core using a YSI 30 conductivity meter (the conductivity is converted to salinity and reported on the Practical Salinity Scale 1978, PSS-78, which is dimensionless).

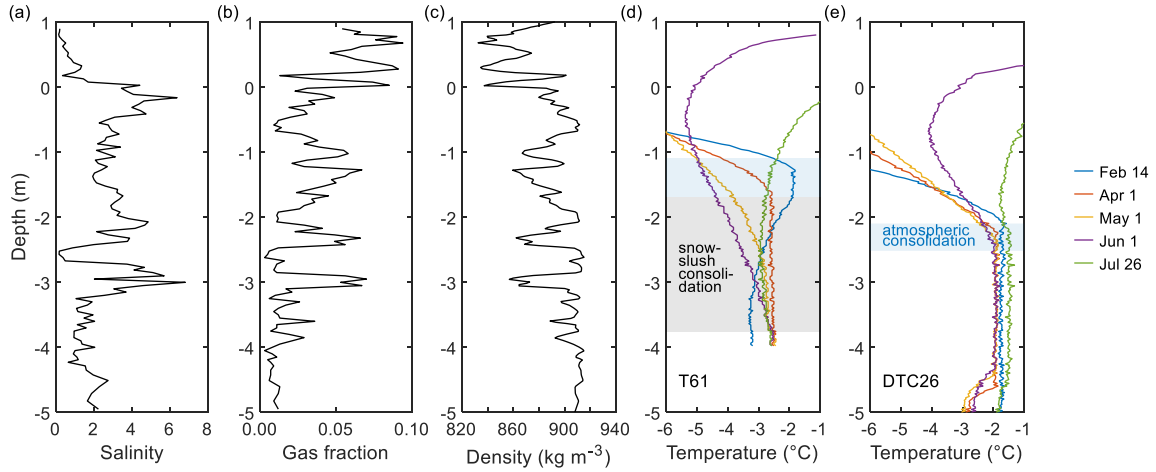

Figure 2. Ice physical parameters and temperatures for Alli's Ridge. (a) Measured sea-ice salinity, (b) estimated relative gas fraction and (c) estimated sea-ice density from in situ measurements of ice salinity from ice coring from July 15 and temperature from ice mass balance buoy DTC26, and measurements of sea-ice density for laboratory temperature of –15°C for the Eastern transect at x = 5.5 m. Vertical ridge temperature profiles from ice mass balance buoys (d) T61 and (e) DTC26 for various dates. Blue-shaded and grey-shaded areas represent atmospheric and snow-slush modes, respectively, of the ridge consolidation.

The estimate of the oceanic heat flux q_w is the difference between the conductive flux inside the ice and the latent flux at the interface. For unconsolidated rubble in a ridge, the conductive heat flux is zero and the latent heat flux is estimated from the change of the keel depth from IMBs. For Alli's Ridge, the ocean heat flux was estimated for DTC26 only, because T61 did not reach the keel bottom. We also estimated the ocean heat flux from IMBs, including T66 installed in level first-year ice (FYI), T56 and T62 in level second-year ice (SYI), and T60 in Fort Ridge, another ice ridge in the Central Observatory.

We estimated snow depth h_{sn} from DTC26 heating measurements (Jackson et al., 2013). Assuming equal conductive fluxes defined by Equation 1 in snow and sea ice at the snow-ice interface, we estimated the value of snow thermal conductivity k_{sn}. For both IMBs, we also estimated snow depth from the heat balance using air ambient temperature T_a, snow-ice interface temperature T_{si}, and the conductive heat flux at the ice surface as:

$$h_{sn} = \frac{k_{sn}(\min(T_a, 0) - T_{si})}{k_{si}\,\partial T_i/\partial z_i} \quad (3)$$

The assumption of equal heat fluxes within ice surface and snow cover is valid only over a substantial time period, as it involves time lag related to sensible heat of snow. To deal with this limitation, we used time-averaging for the estimates of snow depth.

We assumed that snow melt, detected as a decrease of snow depth, and melt of the keel can provide low-saline slush and meltwater for ridge consolidation. We used this assumption to estimate the corresponding latent heat fluxes from the refreezing in the water-filled ridge rubble voids. Based on the snow depth h_{sn}, estimated from IMBs, we calculated the snow refreezing heat flux q_{sn} for ridge as:

$$q_{sn} = \frac{1}{\eta} L_{si} \rho_{sn} \, dh_{sn}/dt, \quad (4)$$

where ρ_{sn} is the snow density, estimated from the heat flux balance at the snow-ice interface as 350 kg m^{-3}. Based on the keel depth h_k, estimated from DTC26, we calculated the keel meltwater refreezing heat flux q_k for the ice ridge as:

$$q_k = \frac{1}{\eta} \rho_{si} L_{si} \, dh_k/dt \quad (5)$$

Both refreezing heat fluxes for snow q_{sn} and keel q_k were estimated assuming one-dimensional transfer, excluding horizontal transfer of meltwater with corresponding meltwater redistribution.

Ridge hydrostatic equilibrium

Many sensors and techniques used to determine sea-ice mass balance measure ice draft and freeboard relative to the water level. Such data do not allow to distinguish between surface and bottom growth and melt. This limitation is valid for airborne (ALS) and terrestrial laser scanning (TLS), remotely operated underwater vehicles (ROV) equipped with sonar, ground-based (GEM) or airborne electromagnetic-induction (AEM) soundings. On the other hand, some measuring devices including IMB buoys and ablation stakes (Perovich et al., 2003) can distinguish between surface and bottom melt.

In this study, we combined both types of ridge measurements from drilling and IMBs to calculate a hydrostatic balance of the ridge. This approach allows to distinguish ridge sail and keel melt which allows relating these processes to atmospheric and oceanographic measurements. Due to the multi-layered structure of ice ridges, calculating such equilibrium requires a number of measurements and assumptions, and aims to estimate the position of the waterline z_w relative to the frame of reference fixed to the sea ice. For each time interval, we assumed that gravity and buoyancy forces acting on the ice ridge are balanced. The gravity force includes the weight from snow, sail, consolidated layer, and unconsolidated rubble. We assumed that sail and rubble have a constant macroporosity equal to the average initial rubble macroporosity η, measured by ice drilling in winter. We estimated sea-ice density for the sail ($\rho_{si,s}$), consolidated layer ($\rho_{si,c}$) and keel ($\rho_{si,k}$) based on laboratory measurements of sea-ice density and salinity and temperature measurements from IMBs as 855, 890, and 900 kg m^{-3}, respectively (**Figure 2**a). The sail melt $\Delta h_s = h_s - h_s(t_0) - z_w$ and snow depth h_{sn} were estimated using continuous temperature measurements from IMBs. The initial and final draft of the consolidated layer h_c was assumed to be equal to the average values from ice drilling in winter and summer. The unknown keel melt Δh_k was assumed to be proportional to the estimates of the ocean heat flux from buoys installed in level ice. The total buoyancy force includes forces from the immersed consolidated layers and rubble. The result of hydrostatic balance gives a position of waterline z_w at any time relative to its initial position at the interface of the sail and the consolidated layer:

$$h_{sn}\rho_{sn} + h_s(1-\eta)\rho_{si,s} + h_c\rho_{si,c} + (h_k - h_c)(1-\eta)\rho_{si,r} = h_c\rho_w + (h_k - h_c)(1-\eta)\rho_w, \quad (6)$$

where ρ_{sn} is the snow density assumed at 350 kg m^{-3}, and ρ_w is the seawater density assumed at 1020 kg m^{-3}.

This balance has three unknown parameters: the waterline position in relation to the initial position $z_w(t)$, the total keel melt $\Delta h_k(t_{end})$ and the total growth of the consolidated layer $\Delta h_c(t_{end})$. It can be solved by using measurements of the final thickness of the consolidated layer h_c and the ridge keel h_k relative to the final waterline position as:

$$h_c(t_{end}) = h_c(t_0) + \Delta h_c(t_{end}) + z_w(t_{end}), \quad (7)$$

$$h_k(t_{end}) = h_k(t_0) + \Delta h_k(t_{end}) + z_w(t_{end}), \quad (8)$$

where $h_{c,0}$ and $h_{k,0}$ are the initial thicknesses of the consolidated layer and ridge keel.

Results and discussion

In the first part of this section, we present the temporal evolution of the ridge morphology, including the changes in snow depth, sail height, keel draft and consolidated layer thickness, and estimates of ridge macroporosity. We also show observations of the ridge temperatures from ice mass balance buoys, which allowed us to study spatial variability and temporal evolution of ridge consolidation. In the second part, we present results of full-year hydrostatic equilibrium balance and its implications on observations of ice melt, allowing to distinguish keel melt and consolidated layer growth from the corresponding changes in draft. In the third part, we present an analysis of ridge thermodynamics by comparing heat fluxes within the ice ridge and fluxes of the main potential contributors to the rapid consolidation of the ridge. We also present estimates of snow, sail, and keel melt to examine which mechanism was responsible for observed stages of consolidation. Finally, we discuss potential mechanisms behind the observed ridge keel consolidation.

Ridge morphology

Here we describe the seasonal evolution of the ridge morphology including keel depth, consolidated layer thickness and macroporosity. We focus on the middle transect across Alli's Ridge with two IMBs and drilling both in winter (January–February) and summer (July). During the winter season, the keel depth along the middle transect ranged from 4.3 m to 7.2 m with a mean value of 5.6 ± 0.8 m (**Figure 3**a); during the summer season, it ranged from 2.2 m to 5.8 m with a mean value of 4.7 ± 1.0 m. In winter, the consolidated layer thickness was 0.5–2.8 m with a mean value of 1.7 ± 0.6 m and in summer, 2.2–5.6 m with a mean value of 3.9 ± 1.1 m. During January–July the fraction of consolidation (h_c/h_k) increased from 32 ± 16% to 84 ± 21%. In summer, the central part of the ridge had a significantly thicker consolidated layer (4.8 ± 0.6 m) than the ridge flanks (3.1 ± 1.0 m), despite being less consolidated in winter. The two IMBs showed different results. The consolidated layer thickness increased at the T61 site from 1.1 m in February to 3.9 m in late July, while at the DTC26 site it only increased from 2.0 m to 2.5 m and then melted to 2.2 m during the same time period. The consolidated layer thickness was 0.7–1.0 m at the T61 location and 2.0 m at the DTC26 location measured from drilling on February 5–17. In the summer season, only 8 of the 25 ridge drilling vertical profiles were not fully consolidated. All unconsolidated ridge profiles were located at the ridge flanks, while fully consolidated profiles were in the middle parts of the ridge with a relatively horizontal keel.

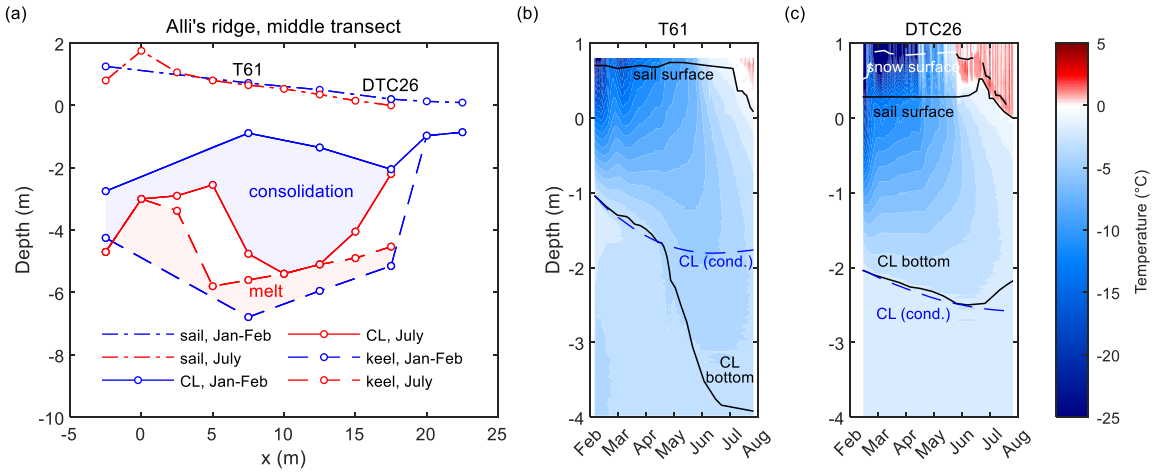

Figure 3. Ridge morphology and temperature evolution. (a) Height of the sail surface, depth of the consolidated layer (CL), and keel for winter and summer season across Alli's Ridge. Contour plots of temperatures from the two ice mass balance buoys (b) T61 and (c) DTC26, with sail and consolidated layer depth (black lines) estimated from temperatures and consolidated layer thickness (blue dashed

line) estimated from the vertical conductive heat flux using Equations (1) and (2).

The initial macroporosity of the keel rubble, estimated from the balance of conductive and latent heat fluxes using Equations (1) and (2), was 43% for T61 and 46% for DTC26. The average rubble macroporosity for the middle transect, from drillings in January–February, was 29 ± 15%, while the total keel macroporosity (including the consolidated layer) was 22 ± 8%. Høyland (2002) also observed higher values of the consolidated layer depth and lower macroporosity from ridge drilling than from temperature measurements. In July, the total ridge macroporosity reduced to 2 ± 4% for the middle transect and 3 ± 4% for all three transects with a maximum value of 14%, which was located at a ridge flank (see **Figure S3**).

Sources of under-ice slush

Snow plays an important role in sea-ice thermodynamics by insulating it from the atmosphere and providing a source of snow-slush and meltwater. During winter, snow-slush is typically formed through the flooding of the ice surface. Snow depth was measured manually along transects in the Central Observatory (Nicolaus et al., 2022); by the beginning of April, level ice had accumulated 0.14 m of snow, while large ridges accumulated 0.63 m (Itkin et al., 2023). For level FYI and SYI, Salganik et al. (2023) reported maximum snow depth of 0.21 m and 0.19 m at the corresponding coring sites, respectively. We estimated the temporal evolution of snow depth above Alli's Ridge from February to July using in-situ and heated temperature measurements from DTC26. From the end of February until the end of May, snow depth at DTC26 was 0.56 to 0.62 m, after which it gradually decreased to 0.4 m by mid-June and 0.1 m by end of June. In July, there was only a surface scattering layer left with a thickness of 0.09 to 0.22 m (**Figure 4**b). The snow depth estimated from T61 temperature measurements increased from February until mid-April to 0.9 m, after which it started to decrease, reaching 0.6 m by mid-May (**Figure 4**a). During March–April, the estimate of snow thermal conductivity from heat balance at the snow-ice interface was increasing from 0.3 to 0.5 W m^{-1} K^{-1}. For estimates of snow depth at the T61 site, we used a constant value for snow thermal conductivity of 0.4 W m^{-1} K^{-1} to fit the observations of estimated and measured snow depth for the DTC26 site before the warm air intrusion on 15–21 April. This value of thermal conductivity corresponds with a snow density of 350 kg m^{-3} (Calonne et al., 2011). Macfarlane et al. (2021) manually measured bulk snow density above level FYI on April 16 as 300 kg m^{-3}, while 0.87 m thick snow above Fort Ridge on February 21 had an average density of 360 kg m^{-3}. The snow depth was also measured manually across the middle transect using a Magnaprobe from January to July. Snow depth at the DTC26 site was representative for the whole middle transect, increasing from 0.02 m in January to 0.5 m in February and April, and then decreasing to 0.24 m in June and to 0.04–0.15 m in July (**Figure 4**b). At T61, snow depth was substantially higher with 0.98 m in April and 0.44 m in June (**Figure 4**a). For a ridge macroporosity of 29% and a snow density of 350 kg m^{-3}, the corresponding consolidated layer thickness equivalent of snow water equivalent would be about 0.6–1.2 m.

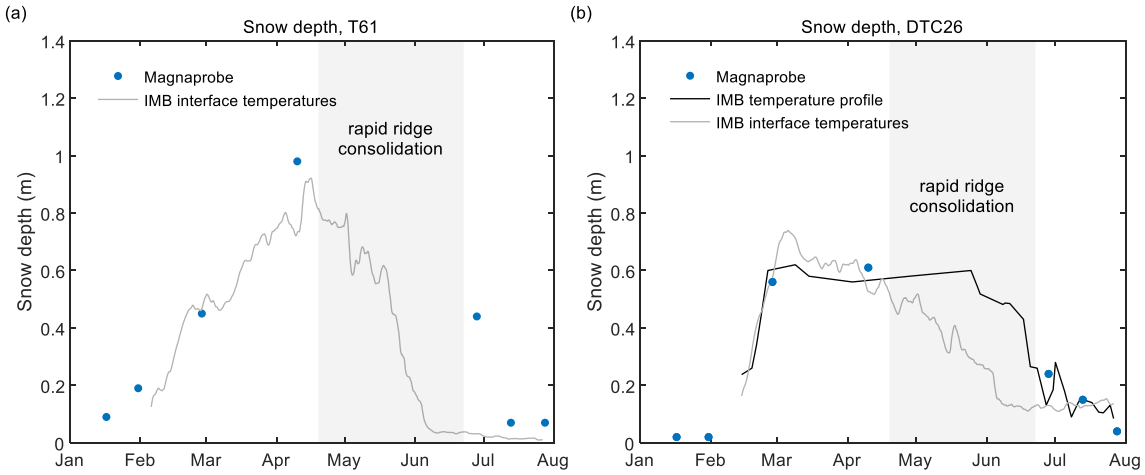

Figure 4. Snow depth estimates from the two ice mass balance buoys T61 and DTC26. (a) Snow depth for T61 was estimated only from interface temperatures (grey line) due to insufficient thermistor

string length. (b) Snow depth for DTC26 was estimated from the temperature profile (black line) by locating the depth with the largest temperature gradient change and from air-snow, snow-ice, and ice-water interface temperatures (grey line). Snow depth estimates from interface temperatures were smoothed using a running average filter with 15-day window. Grey-shaded areas represent the period of rapid ridge consolidation.

Figure 4 also shows the manual snow depth measurements using the Magnaprobe. While these data are very accurate, they were limited by the site accessibility and have substantial observational gaps, including the time of rapid ridge consolidation. The temperature profiles of the snowpack determined from IMBs also provide accurate estimates of the temporal evolution of snow depth, but are limited to the buoy location. The estimates from DTC26 temperature profiles agree well with the Magnaprobe values of snow depth around the buoy. Magnaprobe snow depth measurements across the ridge drilling transect also show that the DTC26 site was representative for Alli's Ridge. The estimates of snow depth from IMB interface temperatures, applied to both DTC26 and T61, are less accurate, as they require knowledge of snow thermal conductivity and temporal averaging to compensate effects of thermal inertia of snowpack. Nevertheless, we provide estimates from all available methods to provide best estimates of temporal evolution of snow depth at different ridge locations.

To validate our estimates of snowmelt evolution, we compared them with similar observations on level ice sites. Using IMBs installed at level FYI and SYI coring sites, we identified snowmelt onset on May 3–9, 2020. Snow completely melted at level FYI and SYI coring sites between May 28 and June 2, while there was still a substantial layer of surface scattering layer of 4–8 cm in June and July (Salganik et al., 2023). We first observed melt ponds in satellite imagery on May 28 (Webster et al., 2022) and at IMBs installed in level ice on May 27. These observations agree with our estimates of snow depth evolution for ridges, indicating intensive snow melt in May.

The warming event from April 15 to 21 (Rinke et al., 2021) substantially affected thermal characteristics of snow by decreasing its thermal resistance. Meanwhile, based on DTC temperature and heated temperature measurements, the snow depth before and after that event remained unchanged. Clemens-Sewall et al. (2023) estimated the average snow loss to leads as only 0.01 m of the snow water equivalent during the warming event.

Wagner et al. (2022) showed that during MOSAiC there was a linear increase of cumulative snowfall from October 2019 until May 2020, while the snow water equivalent along transects did not increase at the same rate (Itkin et al., 2023), indicating a substantial loss of snow in ridge sails, and frozen and open leads. Meanwhile, Déry and Tremblay (2004) estimated 80% efficiency of open leads in trapping blowing snow. In this section we showed that there was enough snow above the ridge to support a substantial snow contribution to the rapid ridge consolidation, which occurred in April–June when most of the snow was removed from the sea ice.

Ridge hydrostatic equilibrium

Repeated ice drilling, the most common way to measure the ice thickness change, does not allow to distinguish between surface and bottom ice melt. The location of ridge freeboard depends on sail and keel melt, consolidation, and snow thickness. Generally, consolidation has the largest contribution to the ridge surface uplift. The ridge and surrounding level ice may bend resisting the hydrostatic equilibrium due to the higher ice volume increase of level ice during the winter season.

Based on ice drilling along the middle transect of Alli's Ridge, the decrease of keel draft from January and February to July was in the range of 0.8 to 1.6 m, with an average value of 0.9 ± 0.8 m for the 3 sites visited during both seasons. At the T61 site, the keel draft decreased by 1.2 m, while the sail height only decreased from between 0.70 m and 0.73 m to 0.65 m. For the 4 sites visited during both seasons, the average ridge sail height decreased from 0.7 ± 0.4 m in winter to 0.5 ± 0.4 m in summer.

The measurements from IMBs can identify the sail and keel melt directly. Sail melt at the end of July was 0.52 m at the DTC26 site and 0.66 m at the T61 site. The initial sail height was 0.2 m for the DTC26 and 0.7 m for the T61 sites. The representative cross-section of Alli's Ridge, with sail height of 0.7 m, consolidated layer thickness of 1.7 m, and keel depth of 5.6 m during winter and sail height of 0.6 m, consolidated layer thickness of 3.9 m, and keel depth of 4.7 m during summer, were both in hydrostatic

equilibrium. Here we also assume that the macroporosities of the sail and keel are equal to the average rubble macroporosity of 29%, measured by ice drilling.

We estimated the contribution to the ridge draft evolution from snow, sail, keel melt, and consolidation using Equations 3–5. We used the estimate of snow depth from DTC26 and sail melt from T61 temperature profiles. For the consolidated layer thickness, we used the estimate from T61, normalized to fit the average initial (1.7 m) and final (3.9 m) consolidated layer draft measured from drilling. For keel melt, we used estimates of ocean heat flux from IMBs, installed in level ice and normalized to fit the average initial keel depth of 5.6 m, and the keel melt calculated from the hydrostatic equilibrium. The estimated sail melt at the T61 site corresponded to a draft decrease of 0.37 m, the consolidation contributed to a draft decrease of 0.14 m, and the total snow melt gives a 0.02 m draft increase. These estimates mean that consolidation and snow and sail melt were responsible for 0.49 m of the 0.9 m of average draft decrease measured by the end of July. The remaining draft decrease corresponded to the keel melt of 0.33 m by July 26. For comparison, the estimated bottom melt of level FYI at the T66 site was 0.27 m for the same period.

The results of the hydrostatic equilibrium corrected the estimate of the average total consolidation from 2.2 m to 2.8 m due to the lift of the consolidated layer relative to the waterline. This estimate of consolidated layer growth is in good agreement with that from T61, confirming that the site is likely representative for Alli's Ridge. The estimate of the sail height from the hydrostatic equilibrium of 0.64 m agrees with the manually measured sail height of 0.65 m at the T61 site in July. The value of 0.33 m for the total keel melt estimated from the hydrostatic equilibrium equals the measurement of total keel melt from DTC26 using heating temperatures (**Figure 5**b).

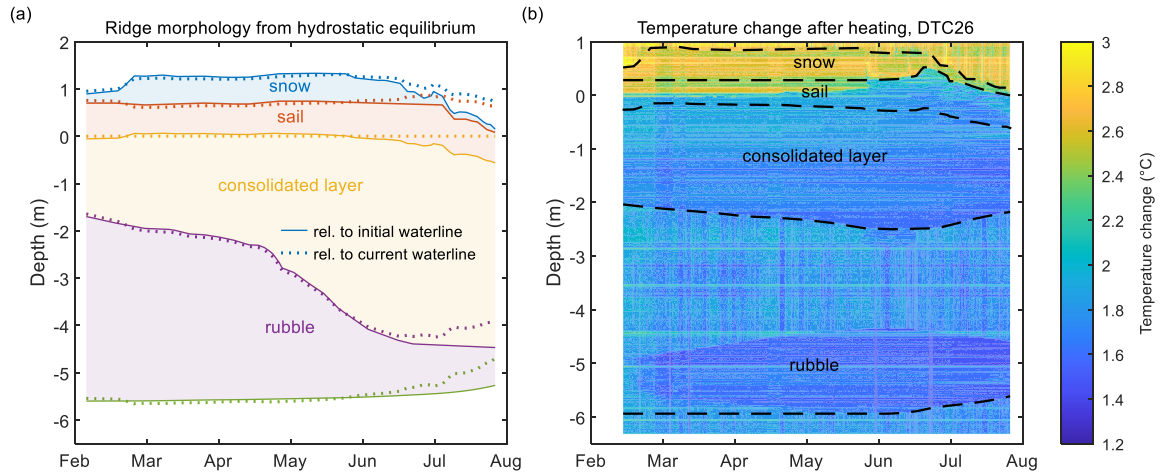

Figure 5. Ridge interface thickness and draft evolution. (a) Evolution of interfaces of snow, sail, consolidated layer, and rubble estimated using hydrostatic equilibrium for the average morphology of Alli's Ridge. The interfaces relative to the initial waterline are shown as solid lines and interface drafts (relative to current waterline) are shown as dotted lines. (b) Contour plot of the temperature change after heating, with estimated interfaces of snow, sail, consolidated layer, and rubble for the ice mass balance buoy DTC26.

The values of ridge macroporosity usually have large variability depending on measuring technique (Høyland, 2002) and location within the ridge (Kharitonov, 2008). For the macroporosity range from 15% to 44%, the estimates of the total keel melt from the hydrostatic equilibrium balance have less than 1% difference, indicating its small sensitivity to the macroporosity values.

Ridge thermodynamics

Ocean heat flux and keel melt

We used DTC26, installed at the southern flank of Alli's Ridge, to measure keel melt and to estimate the corresponding ocean heat flux using Equation 2. Until the beginning of June, keel melt was small, less than the IMB's vertical resolution of 2 cm. From the beginning of June to July 26 the keel was gradually melting with a total melt of 0.33 m and a corresponding average ocean heat flux of 19 W m⁻

^{2} (assuming zero ridge macroporosity). For the same period, the ocean heat flux for level ice calculated as the difference between conductive and latent heat fluxes estimated from IMB measurements had an average value of 20 W m^{-2} (**Figure 6**b). The ridge at the DTC26 site consisted of a consolidated layer, a large 1.8 m deep void, and a 1.6 m thick ice block below (**Figure 5**b). All three ice-water interfaces, at each side of the void and at the bottom of the lowest ice block, experienced similar melt during June and July, making the total ice thickness loss 0.87 m, equivalent to an ocean heat flux of 47 W m^{-2}. The total melt of the consolidated layer at the DTC26 site was 0.32 m, almost identical to the keel melt. This agrees well with the observations by Shestov and Marchenko (2014) of comparable ocean current velocities under level ice and inside large voids in a ridge keel. These observations give insight into the process of ridge keel melt, explaining the faster total melt similar to level ice melt rates for each ice-water interface. Such high internal keel melt at a ridge flank agrees with melt estimates for another ice ridge investigated during the melt period of MOSAiC (Salganik et al., 2022), where melt rates at both ridge flanks and central parts of the ridge were measured. Based on this comparison we assume that at Alli's Ridge the middle parts were also melting more slowly than the flanks (Salganik et al., 2022). These measurements of keel melt are important for the potential sources of meltwater for summer consolidation, which can be located above the keel bottom interface.

From February 5 to April 22 the estimated keel melt at Fort Ridge from T60 heating measurements with a keel depth of 8.5 m was 0.12 m, while for the same period the estimated keel melt at Alli's Ridge from the hydrostatic equilibrium was only 0.04 m. This difference indicates that Alli's Ridge had lower keel melt than some other ridges, including Fort Ridge and Jaridge, investigated during MOSAiC using underwater sonar (Salganik et al., 2022). This lower melt may be related to the relatively shallow and wide keel of Alli's Ridge and the potential sheltering by nearby ridges, located in the direction of the ice drift from Alli's Ridge (**Figure 1**a).

Conductive and latent heat fluxes

Here we analyze the thermodynamics of Alli's Ridge by calculating heat fluxes, related to the ridge consolidation and potential sources of slush and meltwater. Using (1), we calculated conductive heat fluxes for both IMBs installed in the ridge, obtaining average values of 6.1 W m^{-2} for T61 and 5.2 W m^{-2} for DTC26. Salganik et al. (2021) showed that the maximum difference in the conductive heat flux inside nearby ridge blocks and voids is limited by 15% for 50 cm thick blocks. To minimize the potential errors from the presence of horizontal conductive heat fluxes, we used temperature measurements from a depth of 0.8–1.0 m above the areas with inhomogeneous consolidation. During the winter mode of ridge consolidation, the heat from the interface of sea ice and seawater was transferred by thermal conduction via the consolidated layer, sail, and snow layers to the atmosphere. This heat transfer is balanced by the phase change at the ice-water interface or latent heat of solidification. Assuming a ridge macroporosity in the wide range of 30–50%, there is good agreement between conductive and latent heat fluxes at T61 before April 19 (**Figure 6**a). For T61, a rubble macroporosity of 43% gives equal latent and conductive heat for that period, while for the DTC26, such balance is achieved with a macroporosity of 46%.

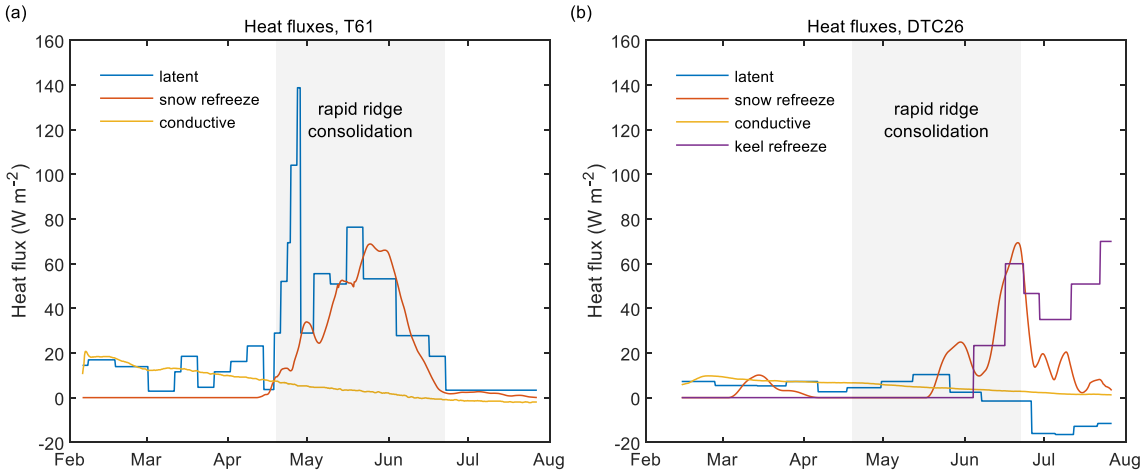

Figure 6. Heat fluxes for Alli's Ridge from ice mass balance buoys. Estimates of latent (blue lines), snow refreeze (red lines), conductive (yellow lines) and keel refreeze (purple lines) heat fluxes at Alli's Ridge from ice mass balance buoys (a) T61 and (b) DTC26. Grey-shaded areas represent the period of rapid ridge consolidation.

During springtime, between April 19 and June 22, there was a substantial increase of the latent heat flux without a corresponding increase of conductive heat flux (**Figure 6**a). During that period, the average latent heat flux was 34 to 56 W m^{-2}, 12–19 times higher than the conductive heat flux given a ridge macroporosity of 30–50%. The corresponding ridge macroporosity for the balance of the two heat fluxes is 3%. This low percentage can be explained by the transfer of snow slush into ridge voids and by the direct heat transfer from the slush (slush consolidation) or low-salinity meltwater to the seawater, which allows the creation of new ice without transferring heat to the atmosphere (meltwater consolidation). From April 10 to 25 at T61, there was a sudden decrease of rubble temperatures by 0.2–0.4°C at the depth of 1.6–3.2 m with a final depth of the consolidated layer by the end of July of 3.8 m, suggesting that over 70% of rapid consolidation was initiated during this period of rubble cooling (**Figure 7**b). These sudden temperature changes in spring may be explained by a rapid transfer of slush to the keel rubble and corresponding negative heat release associated with the dissolution of snow slush by seawater. This heat release can also explain the further freezing due to a strong decrease of macroporosity, which was identified by ice temperatures approaching a linear vertical profile with a delay after the initial temperature decrease of 0.2–0.4°C (**Figure 2**b).

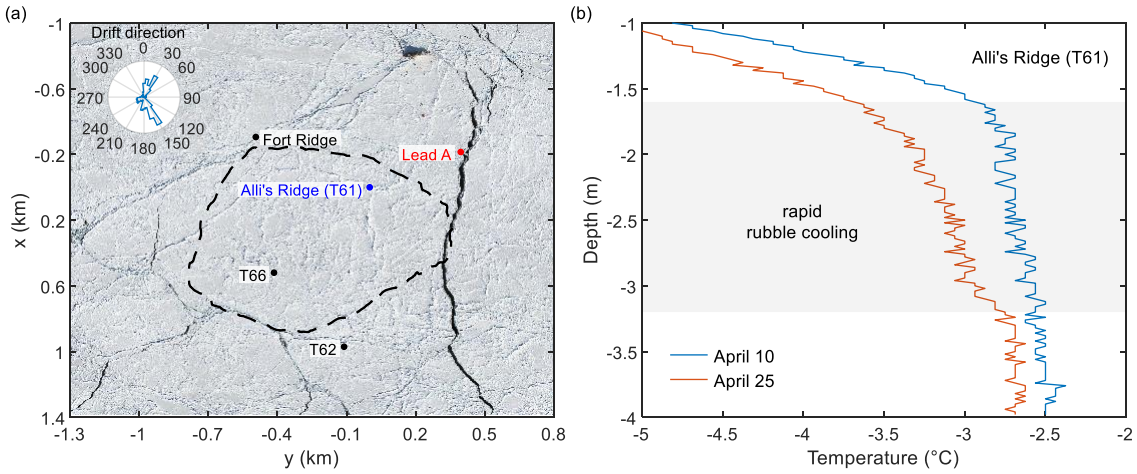

Figure 7. Location of ridges and leads during warming event in April and rubble cooling. (a) Location of Alli's Ridge, Fort Ridge, Lead A, T66 and T62 buoys within the Central Observatory outline on July 1 (black-dashed line) with the background of the aerial image of the ice floe from April 23. The polar histogram shows the frequency of ice drift direction in relation to the displayed ice floe orientation during April 15–23. (b) Vertical ridge temperature profiles from T61 before and after the warming event in April. Grey-shaded area represents the region of rapid cooling of ice rubble.

The sources of the slush and meltwater, which allowed the ridges to consolidate in spring and summer, include slush, keel melt, and surface ice and snow melt. Assuming that all of the local snow loss was transferred into the ridge keel and refrozen into the consolidated layer, we estimated the heat required for the snow or slush to refreeze (**Figure 6**a). For the local snow accumulations above the ridge at T61, the total snow loss of 0.68 m, which mostly occurred after the middle of May, can contribute to around 0.9 m of the consolidation or 40–45% of the rapid ridge consolidation for the rubble macroporosity of 29%. The keel melt for Alli's Ridge was estimated at 0.33 m, while the rapid increase of the consolidated layer was 2.1 m. Considering ridge macroporosity of 29%, the keel melt can contribute to 0.8 m of the consolidated layer, or around 40% of rapid consolidation. Meanwhile, the heat fluxes, related to the meltwater production from snowmelt and keel melt, were increasing only after mid-May, and cannot balance the ridge consolidation from mid-April to mid-May (**Figure 6**b).

Based on our depth estimate for rapid ridge consolidation of 2.1 m, the average final ridge thickness of 5.2 m and the average rubble macroporosity of 29%, we find that 12% of the total ridge volume in July

was associated with the rapid consolidation mode, possibly associated with slush and meltwater. Meanwhile, Lange et al. (in press) estimated the contribution of snowmelt for Alli's Ridge as 8 ± 4 % (n = 117) of the total ridge ice mass with a snow depth equivalent of 1.3 m. This contribution suggests that our estimates of the rapid consolidation mode are within the limits of the refrozen snowmelt volume estimates based on isotope analysis from Lange et al. (in press). The difference of the mass fraction of ice associated with snow of 8% (Lange et al., in press) relative to the total mass fraction of rapid consolidation of 12% (this study) is similar to the thickness of the rapidly cooled ice during the April 15–21 warming event (1.6 m) relative to the total thickness related to rapid consolidation (2.1 m). The isotope analysis of refrozen leads by Clemens-Sewall et al. (2023) suggested substantial snow transfer into open water during the lead opening and snow redistribution event on April 19–20.

Apparent mechanisms of ridge consolidation

The initial one third of the total consolidation occurred in winter due to heat transfer from the seawater through the ice and snow to the atmosphere. Sea-ice ridges are usually consolidating up to two times faster than surrounding level ice because only the ridge void volume (defined by its macroporosity) needs to be frozen during this process. The ratio of consolidated layer thickness h_c and level ice growth Δh_i was described as a function of ridge macroporosity being equal to $\eta^{-0.5}$ by Leppäranta and Hakala (1992). This estimate is based on the heat balance between conductive and latent heat fluxes during atmospheric cooling. In most field observations, the level ice growth Δh_i is substituted by the total level ice thickness h_i, which implies equal initial thickness for ridge and level ice. The h_c/h_i ratio is usually increasing in time approaching a value of 1.6–1.8 (Salganik et al., 2020) based on field measurements from ice drilling by Leppäranta et al. (1995), Blanchet (1998) and Høyland (2002). Using thermal drilling, Kharitonov (2008) found the h_c/h_i ratio equal to 0.8–1.6 for ridges with a keel macroporosity of 10–30%. The simplified $h_c/\Delta h_i$ ratio by Leppäranta and Hakala (1992) includes a number of assumptions, including similar snow depth for level ice and for ridges, which is not realistic (Liston et al., 2018; Itkin et al., 2023). Despite the aforementioned differences between level ice and ridges, we estimated the $h_c/\Delta h_i$ ratio for Alli's Ridge as 1.4 from February 5 to April 19, which then increased linearly to 6.8 at the onset of FYI bottom melt on May 29. The observed difference in growth rates of ridge and level ice before April 19 corresponds to a ridge macroporosity of 54%, while the values for May 29 correspond to a macroporosity of just 5%. The h_c/h_i ratio was 1.1 before April 19, increased to 2.2 on May 29 and reached 3.1 on July 27. Meanwhile, using a simplified model from Leppäranta and Hakala (1992), the estimate of the h_c/h_i ratio based on the measured macroporosity of 29–46% is only 1.5–1.9. This estimate indicates that Alli's Ridge was consolidating relatively slowly before April 19 (likely due to 3-times-thicker snow than for level ice), while the total consolidation rates after summer were approximately 2-times higher than in previous studies.

We showed that nearly two-thirds of the total consolidated layer growth was related to an abrupt increase in rates of consolidation, despite no change in conductive heat fluxes to the atmosphere. The beginning of rapid consolidation in mid-April coincided with a period of high winds and air temperatures (Rinke et al., 2021) and with lead formation and dynamics at the MOSAiC Central Observatory. We surmise that rapid consolidation associated with potential strong decrease of ridge macroporosity (from 29–46% to 3%) was related to the transfer of snow through open leads (Clemens-Sewall et al., 2023) to the ridge keel rubble. During the April 23 warming event, Alli's Ridge was located within 0.4 km of a continuous 20 m wide lead (**Figure 7**a). Clemens-Sewall et al. (2023) reported that significant snow loss into leads occurred on April 19–20, corresponding to 6–10% of annual snow precipitation. Due to high air temperatures reaching −2°C, this lead remained open for 2 days. At the same time the estimated lead fractions of 0.02 and 0.03 within 1 km and 50 km, respectively, around *Polarstern* indicate the presence of other leads in the vicinity of Alli's Ridge. After the lead refreezing, Clemens-Sewall et al. (2023) estimated by isotope analysis the snow contribution as 68% of total lead ice volume. The snow water equivalent was 35 cm, which was equivalent to 65–100% of the precipitation during the lead opening. From previous observations, isotope analysis for level ice showed that formation of snow-ice via slush refreezing can decrease isotope composition with 4% of snow mass fraction for first-year ice (Lange et al., 2021). In this study, we show that the meltwater-related rapid consolidation of Alli's Ridge started at the same time as snow transfer into open leads, supporting the significance of snow contribution for the ridge consolidation.

However, this period is also related to when the MOSAiC floe drifted into more Atlantic-influenced waters, and the ocean surface salinity increased and temperatures decreased (Rabe et al., 2022). Whether these changes also affected the speed of consolidation we cannot deduce from the available observations. A potential effect exists if lower-salinity seawater were to be trapped in the keel cavities and only slowly replaced by saltier and colder ambient seawater. However, because the seawater temperature only changed by about 0.1°C this potential effect would not have contributed to the described rapid consolidation.

The third mechanism of consolidation is related to the refreezing of meltwater from snow, sail and keel melt transferred to the keel rubble. This mechanism was observed much later in the season in July at the peak of the surface melt, when another ridge (Jaridge) was studied through coring and the stable oxygen isotopic properties of ice cores (Lange et al., in press). Lange et al. (in press) estimated the contribution of snowmelt as 8 ± 4% of the total ridge ice mass with a snow depth equivalent of 1.3 m. This finding supports the hypothesis that the rapid mode of consolidation is linked not only to keel melt but also to snowmelt.

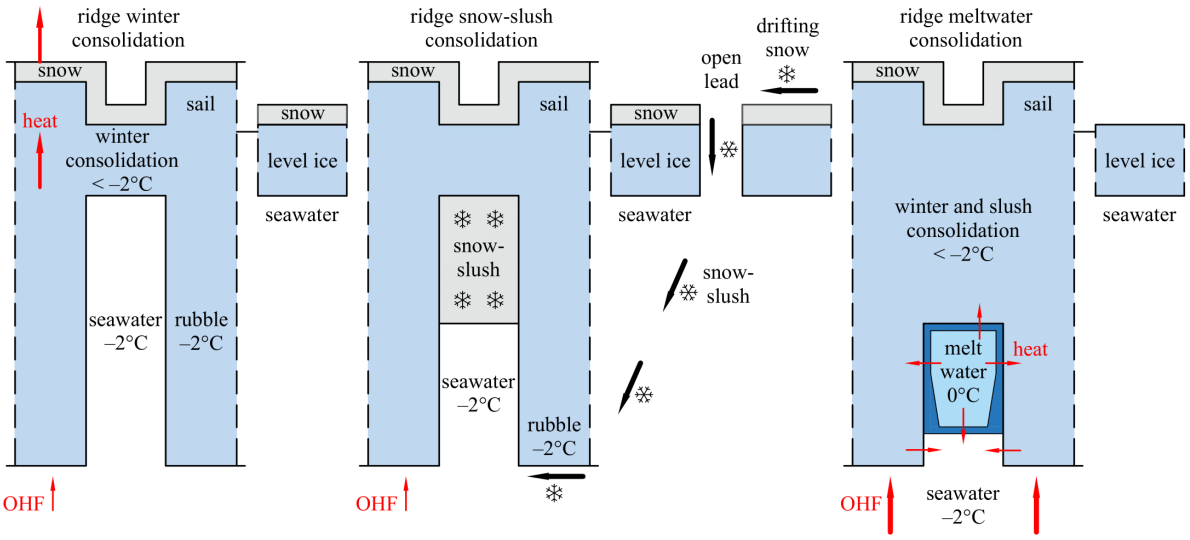

Figure 8. Mechanisms of ridge consolidation. Schematic of different consolidation mechanisms for first-year ridges observed during MOSAiC and associated heat fluxes resulting in consolidation. Each of the three illustrations represents a unit void in a sea-ice ridge, surrounded by two ice blocks. Blue-shaded areas are associated with sea ice grown via atmospheric cooling, grey-shaded areas are associated with snow and snow-slush, and cyan and dark-blue shaded areas are associated with fresher meltwater and refrozen meltwater. The red arrows represent the heat fluxes including the ocean heat flux (OHF), while the black arrows represent snow-slush mass transfer.

The model by Marchenko (2022) predicted full consolidation of a ridge with an initial consolidated layer of 2.0 m, macroporosity of 30%, and a keel depth of 10 m after 431 days. In his model, the summer consolidation of an ice ridge is proportional to the ocean heat flux, which was set to 20 W m^{-2}. The consolidation of a ridge with properties similar to Alli's Ridge should take around 110 days to fully consolidate using the model from Marchenko (2022), while according to our observations it occurred in about 65 days. However, the ocean heat flux started to melt the keel at DTC26 only at the beginning of June, with an average ocean heat flux of 18 W m^{-2} from June 4 to July 26. During this period, the consolidated layer grew from 3.5 to 3.9 m based on T61 measurements, indicating that keel melt contribution likely had at maximum a contribution of about 15% to the total ridge consolidation of 2.8 m. This limited contribution indicates that the refreezing of keel melt was not the mechanism that contributed to the rapid consolidation of Alli's Ridge in April–May.

The sea-ice salinity measurements provide additional evidence of the high importance of snow for the consolidation of Alli's Ridge. The salinity of a sea-ice ridge is usually similar to the salinity of surrounding level ice (Shafrova and Høyland, 2008; Salganik et al., 2021). For Alli's Ridge we measured a bulk salinity of 2.3 and a salinity at 3.2–5.0 m depth of 1.5 in June (**Figure 2**a). The ridge

was formed from lead ice with a bulk salinity of 4.8 and SYI with a bulk salinity of 2.1 measured in February and January (Salganik et al., 2023).

By describing several mechanisms of ridge consolidation, this study has expanded the number of factors that need to be considered for ridge consolidation. For atmospheric consolidation, ridge macroporosity and snow depth distribution have already been described as the key factors (Salganik et al., 2021). For snow-slush consolidation, the presence of open leads defined by air temperatures during spring season is important, while the amount of drifted snow into leads depends largely on wind speed. For meltwater consolidation, studying turbulence around ridge keels is important, as turbulence defines both ridge melt rates and influences the presence of meltwater inside ridge keel voids. The fraction of ridges that experience snow-slush or meltwater consolidation is not yet known, but the improvement in measurement techniques such as ice mass balance buoys and electromagnetic induction sounding may give such estimates in the future. On the other hand, ridges can be sinks of surface meltwater, thus gaining ice mass at a time of the year when the ice is otherwise melting, which in turn can slow their melt due to lower macroporosity. Whether any of these processes need to be represented in sea ice models needs to be examined; given the large fraction of ice volume that resides in these ice formations, their correct representation is likely important for accurate projections of future Arctic sea ice.

Conclusions

In this study, we examined the evolution of the morphology of a first-year Arctic sea-ice ridge from formation in winter to advanced melt in summer. We have identified and described three different mechanisms of ridge consolidation (congelation, snow-slush, and meltwater) and also described them in their seasonal context.

During winter, consolidation is characterized by ice growth due to heat transfer from seawater through the ice and snow to the cold atmosphere as a heat sink. This heat transfer typically increases the consolidated layer thickness to about double the level ice thickness. The summer melt mode is represented by ice growth due to refreezing of low-salinity surface, snow, and keel meltwater in ridge keel voids. Unlike level ice, ridge rubble is isothermal and melts at any substantial ocean heat flux, which provides a source of low-salinity meltwater (in addition to surface snow and ice melt), contributing to ridge consolidation in summer, while the interior of the keel provides a heat sink to support ice formation from low-salinity meltwater when it meets rubble that is below its salinity-determined freezing point.

To our surprise, we observed very rapid consolidation at a time of year when conductive heat fluxes did not increase, nor was meltwater present based on the observations available. This change in consolidation was initiated at the time of a synoptic event of a few days duration with high winds, high air temperatures, ice deformation and the formation of leads. Clemens-Sewall et al. (2023) showed that large amounts of recently precipitated snow (65–100%) were blown into open leads in that short period; we surmise that part of this snow could have entered the ridge keel from an adjacent lead. This is supported by the sudden temperature decrease (0.2–0.4°C) of the ridge rubble at a depth of 1.6–3.2 m during the event. Incorporation of snow into the ridge keel is supported by strongly negative stable oxygen isotopic signatures (8% snow volume fraction equivalent) in an ice core collected from the same ridge (Lange et al., in press). The observed conductive heat fluxes can support such rapid consolidated layer growth only with lower macroporosity which could have been generated with snow-slush.

We have also shown that rapid consolidation occurs primarily in the interior of ridge keels, while ridge flanks are not experiencing slush or meltwater refreezing and only appear to consolidate in winter. At the same time the macroporosity of the interior of the ridge keel decreased substantially, while the flanks still retained some macroporosity. While Lange et al. (in press) assumed that snow melt had caused the incorporation of snow meltwater into the ridge keel, we have surmised here instead that the timing of the sea-ice deformation events and the atmospheric conditions suggest that snow-slush from leads are the primary source for ridge consolidation.

Our analysis has also revealed that the change of keel draft and the bottom melt of the keel may lag in time substantially. An examination of the evolution of the hydrostatic balance showed that in our case the measured draft change of 0.9 m was accompanied with a bottom keel melt of only 0.3 m. The

remaining change was due to consolidation and surface melt that changed the buoyancy of the ridge.

Summer ridge consolidation is, in addition to transient formation of false bottoms (Smith et al., 2022), an overlooked mechanism of ice formation at a time of year when the ice pack is otherwise melting; this term should thus be considered when meltwater budgets are concerned. The rather rapid consolidation of the void space also has repercussions for biota that may take refuge in the ridge keel cavities (Gradinger et al., 2010; Fernández-Méndez et al., 2018). Given the lack of comprehensive observations of sea-ice ridges, further emphasis should be given to better understand the different mechanisms of consolidation with better temporal coverage of ridge morphology evolution and their links to ridges as a habitat. A valid question is whether any of these processes, given the large volume fraction of deformed ice, need to be better represented in models to improve Arctic sea-ice forecasts.

References

Amundrud, TL, Melling, H, Ingram, G. 2004. Geometrical constraints on the evolution of ridged sea ice. *Journal of Geophysical Research: Oceans* **109**(6): 1–12. doi: 10.1029/2003JC002251

Blanchet, D. 1998. Ice loads from first-year ice ridges and rubble fields. *Canadian Journal of Civil Engineering* **25**(2): 206–219. doi: 10.1139/l97-073

Calonne, N, Flin, F, Morin, S, Lesaffre, B, Du Roscoat, SR, Geindreau, C. 2011. Numerical and experimental investigations of the effective thermal conductivity of snow. *Geophysical Research Letters* **38**(23): 1–6. doi: 10.1029/2011GL049234

Clemens-Sewall, D, Polashenski, C, Frey, MM, Christopher, J, Granskog, MA, Macfarlane, AR, Fons, SW, Hutchings, JK, Albedyll, L Von, Arndt, S. 2023. Snow loss into leads in Arctic sea ice: minimal in typical wintertime conditions, but high during a warm and windy snowfall event. *Geophysical Research Letters*, in press. doi: 10.22541/essoar.167751637.76975855/v1

Cox, GFN, Weeks, WF. 1983. Equations for determining the gas and brine volumes in sea-ice samples. *Journal of Glaciology* **29**(102): 306–316. doi: 10.3189/S0022143000008364

Déry, SJ, Tremblay, L-B. 2004. Modeling the effects of wind redistribution on the snow mass budget of polar sea ice. *Journal of Physical Oceanography* **34**(1): 258–271. doi: 10.1175/1520-0485(2004)034<0258:MTEOWR>2.0.CO;2

Duncan, K, Farrell, SL. 2022. Determining variability in Arctic sea ice pressure ridge topography with ICESat-2. *Geophysical Research Letters* **49**(18): 1–10. doi: 10.1029/2022GL100272

Fernández-Méndez, M, Olsen, LM, Kauko, HM, Meyer, A, Rösel, A, Merkouriadi, I, Mundy, CJ, Ehn, JK, Johansson, AM, Wagner, PM, Ervik, Å, Sorrell, BK, Duarte, P, Wold, A, Hop, H, Assmy, P. 2018. Algal hot spots in a changing Arctic Ocean: sea-ice ridges and the snow-ice interface. *Frontiers in Marine Science* **5**. doi: 10.3389/fmars.2018.00075

Gradinger, R, Bluhm, B, Iken, K. 2010. Arctic sea-ice ridges—Safe heavens for sea-ice fauna during periods of extreme ice melt? *Deep Sea Research Part II: Topical Studies in Oceanography* **57**(1–2): 86–95. doi: 10.1016/j.dsr2.2009.08.008

Granskog, MA, Fer, I, Rinke, A, Steen, H. 2018. Atmosphere-ice-ocean-ecosystem processes in a thinner Arctic sea ice regime: the Norwegian Young Sea ICE (N-ICE2015) Expedition. *Journal of Geophysical Research: Oceans* **123**(3): 1586–1594. doi: 10.1002/2017JC013328

Hansen, E, Ekeberg, OC, Gerland, S, Pavlova, O, Spreen, G, Tschudi, M. 2014. Variability in categories of Arctic sea ice in Fram Strait. *Journal of Geophysical Research: Oceans* **119**(10): 7175–7189. doi: 10.1002/2014JC010048

Hop, H, Pavlova, O. 2008. Distribution and biomass transport of ice amphipods in drifting sea ice around Svalbard. *Deep Sea Research Part II: Topical Studies in Oceanography* **55**(20–21): 2292–2307. doi: 10.1016/j.dsr2.2008.05.023

Hopkins, MA, Hibler, WD, Flato, GM. 1991. On the numerical simulation of the sea ice ridging process. *Journal of Geophysical Research* **96**(C3): 4809. doi: 10.1029/90JC02375

Høyland, K V. 2002. Consolidation of first-year sea ice ridges. *Journal of Geophysical Research* **107**(C6): 3062. doi: 10.1029/2000JC000526

Høyland, K V. 2007. Morphology and small-scale strength of ridges in the North-western Barents Sea. *Cold Regions Science and Technology*, in press. doi: 10.1016/j.coldregions.2007.01.006

Itkin, P, Hendricks, S, Webster, M, von Albedyll, L, Arndt, S, Divine, D, Jaggi, M, Oggier, M, Raphael, I, Ricker, R, Rohde, J, Schneebeli, M, Liston, GE. 2023. Sea ice and snow characteristics from year-long transects at the MOSAiC Central Observatory. *Elementa: Science of the Anthropocene* **11**(1). doi: 10.1525/elementa.2022.00048

Jackson, K, Wilkinson, J, Maksym, T, Meldrum, D, Beckers, J, Haas, C, Mackenzie, D. 2013. A novel and low-cost sea ice mass balance buoy. *Journal of Atmospheric and Oceanic Technology* **30**(11): 2676–2688. doi: 10.1175/JTECH-D-13-00058.1

Kankaanpää, P. 1997. Distribution, morphology and structure of sea ice pressure ridges in the Baltic Sea. *Fennia - International Journal of Geography* **175**(2): 139–240. Available at https://fennia.journal.fi/article/view/8919.

Katlein, C, Mohrholz, V, Sheikin, I, Itkin, P, Divine, D V., Stroeve, J, Jutila, A, Krampe, D, Shimanchuk, E, Raphael, I, Rabe, B, Kuznetsov, I, Mallet, M, Liu, H, Hoppmann, M, Fang, Y, Dumitrascu, A, Arndt, S, Anhaus, P, Nicolaus, M, Matero, I, Oggier, M, Eicken, H, Haas, C. 2020. Platelet ice under Arctic pack ice in winter. *Geophysical Research Letters* **47**(16). doi: 10.1029/2020GL088898

Kharitonov, V V. 2008. Internal structure of ice ridges and stamukhas based on thermal drilling data. *Cold Regions Science and Technology* **52**(3): 302–325. doi: 10.1016/j.coldregions.2007.04.020

Knust, R. 2017. Polar Research and Supply Vessel POLARSTERN operated by the Alfred-Wegener-Institute. *Journal of large-scale research facilities JLSRF* **3**: A119. doi: 10.17815/jlsrf-3-163

Kovacs, A. 1983. Characterstic of multi-year pressure ridges. Proceedings of Port and Ocean Engineering under Arctic Conditions, POAC'83, Helsinki, Vol. 3: 173–182. Available at https://espis.boem.gov/final reports/1279.pdf.

Krumpen, T, Birrien, F, Kauker, F, Rackow, T, Von Albedyll, L, Angelopoulos, M, Jakob Belter, H, Bessonov, V, Damm, E, Dethloff, K, Haapala, J, Haas, C, Harris, C, Hendricks, S, Hoelemann, J, Hoppmann, M, Kaleschke, L, Karcher, M, Kolabutin, N, Lei, R, Lenz, J, Morgenstern, A, Nicolaus, M, Nixdorf, U, Petrovsky, T, Rabe, B, Rabenstein, L, Rex, M, Ricker, R, Rohde, J, Shimanchuk, E, Singha, S, Smolyanitsky, V, Sokolov, V, Stanton, T, Timofeeva, A, Tsamados, M, Watkins, D. 2020. The MOSAiC ice floe: Sediment-laden survivor from the Siberian shelf. *Cryosphere* **14**(7): 2173–2187. doi: 10.5194/tc-14-2173-2020

Lange, BA, Haas, C, Mucci, A, Beckers, JF, Casey, JA, Duerksen, S, Granskog, MA, Hatam, I, Niemi, A, Reppchen, A, Michel, C. 2021. Contribution of snow to Arctic first-year and multi-year sea ice mass balance within the Last Ice Area. *Journal of Geophysical Research: Oceans* **126**(5): 1–14. doi: 10.1029/2020JC016971

Lange, BA, Katlein, C, Castellani, G, Fernández-Méndez, M, Nicolaus, M, Peeken, I, Flores, H. 2017. Characterizing spatial variability of ice algal chlorophyll a and net primary production between sea ice habitats using horizontal profiling platforms. *Frontiers in Marine Science* **4**. doi: 10.3389/fmars.2017.00349

Lange, BA, Salganik, E, Macfarlane, A, Schneebeli, M, Høyland, KV, Gardner, J, Müller, O, Divine, D V., Kohlbach, D, Katlein, C, Granskog, MA. 2023. Snowmelt contributes to Arctic first-year ice ridge mass balance and rapid consolidation during summer melt. *Elementa: Science of the Anthropocene*, in press.

Lei, R, Cheng, B, Hoppmann, M, Zhang, F, Zuo, G, Hutchings, JK, Lin, L, Lan, M, Wang, H, Regnery, J, Krumpen, T, Haapala, J, Rabe, B, Perovich, DK, Nicolaus, M. 2022. Seasonality and timing of sea ice mass balance and heat fluxes in the Arctic transpolar drift during 2019–2020. *Elementa:*

Science of the Anthropocene **10**(1). doi: 10.1525/elementa.2021.000089

Leppäranta, M, Hakala, R. 1992. The structure and strength of first-year ice ridges in the Baltic Sea. *Cold Regions Science and Technology* **20**(3): 295–311. doi: 10.1016/0165-232X(92)90036-T

Leppäranta, M, Lensu, M, Kosloff, P, Veitch, B. 1995. The life story of a first-year sea ice ridge. *Cold Regions Science and Technology* **23**(3): 279–290. doi: 10.1016/0165-232X(94)00019-T

Leppäranta, M, Manninen, T. 1988. The brine and gas content of sea ice with attention to low salinities and high temperatures. Helsinki, Finland: Finnish Institute of Marine Research. Available at http://aquaticcommons.org/id/eprint/6760.

Liston, GE, Polashenski, C, Rösel, A, Itkin, P, King, J, Merkouriadi, I, Haapala, J. 2018. A distributed snow-evolution model for sea-ice applications (snowmodel). *Journal of Geophysical Research: Oceans* **123**(5): 3786–3810. doi: 10.1002/2017JC013706

Marchenko, A. 2022. Thermo-Hydrodynamics of Sea Ice Rubble. In: *IUTAM Bookseries*. Springer International Publishing. p. 203–223. doi: 10.1007/978-3-030-80439-8_10

Nicolaus, M, Perovich, DK, Spreen, G, Granskog, MA, von Albedyll, L, Angelopoulos, M, Anhaus, P, Arndt, S, Belter, HJ, Bessonov, V, Birnbaum, G, Brauchle, J, Calmer, R, Cardellach, E, Cheng, B, Clemens-Sewall, D, Dadic, R, Damm, E, de Boer, G, Demir, O, Dethloff, K, Divine, D V., Fong, AA, Fons, S, Frey, MM, Fuchs, N, Gabarró, C, Gerland, S, Goessling, HF, Gradinger, R, Haapala, J, Haas, C, Hamilton, J, Hannula, H-R, Hendricks, S, Herber, A, Heuzé, C, Hoppmann, M, Høyland, KV, Huntemann, M, Hutchings, JK, Hwang, B, Itkin, P, Jacobi, H-W, Jaggi, M, Jutila, A, Kaleschke, L, Katlein, C, Kolabutin, N, Krampe, D, Kristensen, SS, Krumpen, T, Kurtz, N, Lampert, A, Lange, BA, Lei, R, Light, B, Linhardt, F, Liston, GE, Loose, B, Macfarlane, AR, Mahmud, M, Matero, IO, Maus, S, Morgenstern, A, Naderpour, R, Nandan, V, Niubom, A, Oggier, M, Oppelt, N, Pätzold, F, Perron, C, Petrovsky, T, Pirazzini, R, Polashenski, C, Rabe, B, Raphael, IA, Regnery, J, Rex, M, Ricker, R, Riemann-Campe, K, Rinke, A, Rohde, J, Salganik, E, Scharien, RK, Schiller, M, Schneebeli, M, Semmling, M, Shimanchuk, E, Shupe, MD, Smith, MM, Smolyanitsky, V, Sokolov, V, Stanton, T, Stroeve, J, Thielke, L, Timofeeva, A, Tonboe, RT, Tavri, A, Tsamados, M, Wagner, DN, Watkins, D, Webster, M, Wendisch, M. 2022. Overview of the MOSAiC expedition. *Elementa: Science of the Anthropocene* **10**(1). doi: 10.1525/elementa.2021.000046

Notz, D. 2005. Thermodynamic and fluid-dynamical processes in sea ice. University of Cambridge. Available at http://mpimet.mpg.de/fileadmin/staff/notzdirk/Notz_PhD_abstract.pdf.

Perovich, DK, Grenfell, TC, Richter-Menge, JA, Light, B, Tucker, WB, Eicken, H. 2003. Thin and thinner: Sea ice mass balance measurements during SHEBA. *Journal of Geophysical Research: Oceans* **108**(3): 1–21. doi: 10.1029/2001jc001079

Peterson, AK, Fer, I, McPhee, MG, Randelhoff, A. 2017. Turbulent heat and momentum fluxes in the upper ocean under Arctic sea ice. *Journal of Geophysical Research: Oceans* **122**(2): 1439–1456. doi: 10.1002/2016JC012283

Pustogvar, A, Kulyakhtin, A. 2016. Sea ice density measurements. Methods and uncertainties. *Cold Regions Science and Technology* **131**: 46–52. Elsevier B.V. doi: 10.1016/j.coldregions.2016.09.001

Rabe, B, Heuzé, C, Regnery, J, Aksenov, Y, Allerholt, J, Athanase, M, Bai, Y, Basque, C, Bauch, D, Baumann, TM, Chen, D, Cole, ST, Craw, L, Davies, A, Damm, E, Dethloff, K, Divine, D V., Doglioni, F, Ebert, F, Fang, Y-C, Fer, I, Fong, AA, Gradinger, R, Granskog, MA, Graupner, R, Haas, C, He, H, He, Y, Hoppmann, M, Janout, M, Kadko, D, Kanzow, T, Karam, S, Kawaguchi, Y, Koenig, Z, Kong, B, Krishfield, RA, Krumpen, T, Kuhlmey, D, Kuznetsov, I, Lan, M, Laukert, G, Lei, R, Li, T, Torres-Valdés, S, Lin, Lina, Lin, Long, Liu, H, Liu, N, Loose, B, Ma, X, McKay, R, Mallet, M, Mallett, RDC, Maslowski, W, Mertens, C, Mohrholz, V, Muilwijk, M, Nicolaus, M, O'Brien, JK, Perovich, D, Ren, J, Rex, M, Ribeiro, N, Rinke, A, Schaffer, J, Schuffenhauer, I, Schulz, K, Shupe, MD, Shaw, W, Sokolov, V, Sommerfeld, A, Spreen, G, Stanton, T, Stephens,

M, Su, J, Sukhikh, N, Sundfjord, A, Thomisch, K, Tippenhauer, S, Toole, JM, Vredenborg, M, Walter, M, Wang, H, Wang, L, Wang, Y, Wendisch, M, Zhao, J, Zhou, M, Zhu, J. 2022. Overview of the MOSAiC expedition: Physical oceanography. *Elementa: Science of the Anthropocene* **10**(1). doi: 10.1525/elementa.2021.00062

Ricker, R, Fons, S, Jutila, A, Hutter, N, Duncan, K, Farrell, SL, Kurtz, NT, Fredensborg Hansen, RM. 2023. Linking scales of sea ice surface topography: evaluation of ICESat-2 measurements with coincident helicopter laser scanning during MOSAiC. *The Cryosphere* **17**(3): 1411–1429. doi: 10.5194/tc-17-1411-2023

Rinke, A, Cassano, JJ, Cassano, EN, Jaiser, R, Handorf, D. 2021. Meteorological conditions during the MOSAiC expedition: Normal or anomalous? *Elementa* **9**(1): 1–17. doi: 10.1525/elementa.2021.00023

Rothrock, DA. 2005. Arctic Ocean sea ice volume: What explains its recent depletion? *Journal of Geophysical Research* **110**(C1): C01002. doi: 10.1029/2004JC002282

Salganik, E, Høyland, KV, Maus, S. 2020. Consolidation of fresh ice ridges for different scales. *Cold Regions Science and Technology* **171**: 102959. doi: 10.1016/j.coldregions.2019.102959

Salganik, E, Høyland, KV, Shestov, A. 2021. Medium-scale experiment in consolidation of an artificial sea ice ridge in Van Mijenfjorden, Svalbard. *Cold Regions Science and Technology* **181**(May 2020). doi: 10.1016/j.coldregions.2020.103194

Salganik, E, Katlein, C, Lange, BA, Matero, I, Lei, R, Fong, AA, Fons, SW, Divine, D, Oggier, M, Castellani, G, Bozzato, D, Chamberlain, EJ, Hoppe, CJM, Müller, O, Gardner, J, Rinke, A, Pereira, PS, Ulfsbo, A, Marsay, C, Webster, MA, Maus, S, Høyland, K V., Granskog, MA. 2023. Temporal evolution of under-ice meltwater layers and false bottoms and their impact on summer Arctic sea ice mass balance. *Elementa: Science of the Anthropocene* **11**(1). doi: 10.1525/elementa.2022.00035

Salganik, E, Lange, B, Katlein, C, Matero, I, Regnery, J, Sheikin, I, Anhaus, P, Høyland, KV, Granskog, MA. 2022. Differential summer melt rates of ridges, first- and second-year ice in the central Arctic Ocean during the MOSAiC expedition. EGU General Assembly 2022. Vienna, Austria. doi: 10.5194/egusphere-egu22-11518

Shafrova, S, Høyland, K V. 2008. Morphology and 2D spatial strength distribution in two Arctic first-year sea ice ridges. *Cold Regions Science and Technology* **51**(1): 38–55. doi: 10.1016/j.coldregions.2007.05.011

Shestov, A, Høyland, K, Ervik, Å. 2018. Decay phase thermodynamics of ice ridges in the Arctic Ocean. *Cold Regions Science and Technology* **152**: 23–34. doi: 10.1016/j.coldregions.2018.04.005

Shestov, A, Marchenko, A. 2014. Properties of Ice Ridge Keels and Sea Currents in their Vicinity in the Barents Sea 22 nd IAHR International Symposium on Ice Properties of Ice Ridge Keels and Sea Currents in their Vicinity in the Barents Sea. : 1–9. doi: 10.13140/2.1.2955.2004

Shupe, MD, Rex, M, Blomquist, B, Persson, POG, Schmale, J, Uttal, T, Althausen, D, Angot, H, Archer, S, Bariteau, L, Beck, I, Bilberry, J, Bucci, S, Buck, C, Boyer, M, Brasseur, Z, Brooks, IM, Calmer, R, Cassano, J, Castro, V, Chu, D, Costa, D, Cox, CJ, Creamean, J, Crewell, S, Dahlke, S, Damm, E, de Boer, G, Deckelmann, H, Dethloff, K, Dütsch, M, Ebell, K, Ehrlich, A, Ellis, J, Engelmann, R, Fong, AA, Frey, MM, Gallagher, MR, Ganzeveld, L, Gradinger, R, Graeser, J, Greenamyer, V, Griesche, H, Griffiths, S, Hamilton, J, Heinemann, G, Helmig, D, Herber, A, Heuzé, C, Hofer, J, Houchens, T, Howard, D, Inoue, J, Jacobi, H-W, Jaiser, R, Jokinen, T, Jourdan, O, Jozef, G, King, W, Kirchgaessner, A, Klingebiel, M, Krassovski, M, Krumpen, T, Lampert, A, Landing, W, Laurila, T, Lawrence, D, Lonardi, M, Loose, B, Lüpkes, C, Maahn, M, Macke, A, Maslowski, W, Marsay, C, Maturilli, M, Mech, M, Morris, S, Moser, M, Nicolaus, M, Ortega, P, Osborn, J, Pätzold, F, Perovich, DK, Petäjä, T, Pilz, C, Pirazzini, R, Posman, K, Powers, H, Pratt, KA, Preußer, A, Quéléver, L, Radenz, M, Rabe, B, Rinke, A, Sachs, T, Schulz, A, Siebert, H, Silva, T, Solomon, A, Sommerfeld, A, Spreen, G, Stephens, M, Stohl, A, Svensson, G, Uin, J, Viegas, J,

Voigt, C, von der Gathen, P, Wehner, B, Welker, JM, Wendisch, M, Werner, M, Xie, Z, Yue, F. 2022. Overview of the MOSAiC expedition: Atmosphere. *Elementa: Science of the Anthropocene* **10**(1). doi: 10.1525/elementa.2021.00060

Smith, MM, von Albedyll, L, Raphael, IA, Lange, BA, Matero, I, Salganik, E, Webster, MA, Granskog, MA, Fong, A, Lei, R, Light, B. 2022. Quantifying false bottoms and under-ice meltwater layers beneath Arctic summer sea ice with fine-scale observations. *Elementa: Science of the Anthropocene* **10**(1). doi: 10.1525/elementa.2021.000116

Timco, GW, Burden, RP. 1997. An analysis of the shapes of sea ice ridges. *Cold Regions Science and Technology* **25**(1): 65–77. doi: 10.1016/S0165-232X(96)00017-1

Tsamados, M, Feltham, DL, Schroeder, D, Flocco, D, Farrell, SL, Kurtz, N, Laxon, SW, Bacon, S. 2014. Impact of variable atmospheric and oceanic form drag on simulations of arctic sea ice. *Journal of Physical Oceanography* **44**(5): 1329–1353. doi: 10.1175/JPO-D-13-0215.1

Tucker, WB, Sodhi, DS, Govoni, JW. 1984. Structure of first-year pressure ridge sails in the Prudhoe region. In: *The Alaskan Beaufort Sea*. Elsevier. p. 115–135. doi: 10.1016/B978-0-12-079030-2.50012-5

Wagner, DN, Shupe, MD, Cox, C, Persson, OG, Uttal, T, Frey, MM, Kirchgaessner, A, Schneebeli, M, Jaggi, M, Macfarlane, AR, Itkin, P, Arndt, S, Hendricks, S, Krampe, D, Nicolaus, M, Ricker, R, Regnery, J, Kolabutin, N, Shimanshuck, E, Oggier, M, Raphael, I, Stroeve, J, Lehning, M. 2022. Snowfall and snow accumulation during the MOSAiC winter and spring seasons. *The Cryosphere* **16**(6): 2373–2402. doi: 10.5194/tc-16-2373-2022

Webster, MA, Holland, M, Wright, NC, Hendricks, S, Hutter, N, Itkin, P, Light, B, Linhardt, F, Perovich, DK, Raphael, IA, Smith, MM, von Albedyll, L, Zhang, J. 2022. Spatiotemporal evolution of melt ponds on Arctic sea ice. *Elementa: Science of the Anthropocene* **10**(1). doi: 10.1525/elementa.2021.000072

WMO. 2014. World Meteorological Organization (WMO) Sea Ice Nomenclature: WMO-No. 259 922. Supplement to Vol. I, II and II, 5th session of JCOMM Expert Team on Sea ice. Tech. rep. doi: 10.25607/OBP-1530

Data accessibility statement

All data used herein are available publicly as listed below:

Granskog, MA, Berge, J, Cottier, F, Divine, DV, Katlein, C, Itkin, P, Olsen, LM, Vogedes, D, De La Torre, PR. 2021. Temperature and heating induced temperature difference measurements from the sea ice mass balance buoy SIMBA 2020T61. PANGAEA. doi: 10.1594/PANGAEA.926580

Granskog, MA, Høyland, KV, De La Torre, PR, Divine, DV, Katlein, C, Itkin, P, Raphael, I, Olsen, LM. 2020. Temperature and heating induced temperature difference measurements from the sea ice mass balance buoy SIMBA 2020T60. PANGAEA. doi: 10.1594/PANGAEA.924269

Haas, C, Hoppmann, M, Tippenhauer, S, Rohardt, G. 2021. Continuous thermosalinograph oceanography along RV POLARSTERN cruise track PS122/2. PANGAEA. doi: 10.1594/PANGAEA.930024

Hoppmann, M, Scholz, D, Arndt, S, Divine, DV, Itkin, P, Katlein, C, Salganik, E. 2022. Temperature and heating induced temperature difference measurements from the sea ice mass balance buoy DTC 26 during MOSAiC 2019/2020. PANGAEA. doi: 10.1594/PANGAEA.951780

Itkin, P, Webster, M, Hendricks, S, Oggier, M, Jaggi, M, Ricker, R, Arndt, S, Divine, DV, von Albedyll, L, Raphael, I, Rohde, J, Liston, GE. 2021. Magnaprobe snow and melt pond depth measurements from the 2019-2020 MOSAiC expedition. PANGAEA. doi: 10.1594/PANGAEA.937781

Kanzow, T, Hoppmann, M, Tippenhauer, S, Rohardt, G. 2021. Continuous thermosalinograph

oceanography along RV POLARSTERN cruise track PS122/3. PANGAEA. doi: 10.1594/PANGAEA.930026

Lange, BA, Salganik, E, Macfarlane, AR, Schneebeli, M, Høyland, KV, Gardner, J, Müller, O, Granskog, MA. 2022. Ridge ice oxygen and hydrogen isotope data MOSAiC Leg 4 (PS122/4). PANGAEA. doi: 10.1594/PANGAEA.943746

Lei, R., Cheng, B., Hoppmann, M., Zuo, G. 2021. Snow depth and sea ice thickness derived from the measurements of SIMBA buoy 2019T62, PANGAEA. doi: 10.1594/PANGAEA.938228

Lei, R, Cheng, B, Hoppmann, M, Zuo, G. 2021. Snow depth and sea ice thickness derived from the measurements of SIMBA buoy 2019T66, PANGAEA. doi: 10.1594/PANGAEA.938134

Macfarlane, AR, Schneebeli, M, Dadic, R, Wagner, DN, Arndt, S, Clemens-Sewall, D, Hämmerle, S, Hannula, H-R, Jaggi, M, Kolabutin, N, Krampe, D, Lehning, M, Matero, I, Nicolaus, M, Oggier, M, Pirazzini, R, Polashenski, C, Raphael, I, Regnery, J, Shimanchuck, E, Smith, MM, Tavri, A. 2021. Snowpit raw data collected during the MOSAiC expedition. PANGAEA. doi: 10.1594/PANGAEA.935934

Neckel, N, Fuchs, N, Birnbaum, G, Hutter, N, Jutila, A, Buth, L, von Albedyll, L, Ricker, R, Haas, C. 2022. Helicopter-borne RGB orthomosaics and photogrammetric Digital Elevation Models from the MOSAiC Expedition. PANGAEA. doi: 10.1594/PANGAEA.949433

Oggier, M, Salganik, E, Whitmore, L, Fong, AA, Hoppe, CJM, Rember, R, Høyland, KV, Divine, DV, Gradinger, R, Fons, SW, Abrahamsson, K, Aguilar-Islas, AM, Angelopoulos, M, Arndt, S, Balmonte, JP, Bozzato, D, Bowman, JS, Castellani, G, Chamberlain, E, Creamean, J, D'Angelo, A, Damm, E, Dumitrascu, A, Eggers, SL, Gardner, J, Grosfeld, L, Haapala, J, Immerz, A, Kolabutin, N, Lange, BA, Lei, R, Marsay, CM, Maus, S, Olsen, LM, Müller, O, Nuibom A, Ren, J, Rinke, A, Sheikin, I, Shimanchuk, E, Snoeijs-Leijonmalm, P, Spahic, S, Stefels, J, Torres-Valdés, S, Torstensson, A, Ulfsbo, A, Verdugo, J, Vortkamp, M, Wang, L, Webster, M, Wischnewski, L, Granskog, MA (2023): First-year sea-ice salinity, temperature, density, oxygen and hydrogen isotope composition from the main coring site (MCS-FYI) during MOSAiC legs 1 to 4 in 2019/2020. PANGAEA. doi: 10.1594/PANGAEA.956732

Rex, M, Hoppmann, M, Tippenhauer, S, Rohardt, G. 2021. Continuous thermosalinograph oceanography along RV POLARSTERN cruise track PS122/4. PANGAEA. doi: 10.1594/PANGAEA.930027

Salganik, E, Lange, BA, Divine, DV, Itkin, P, Katlein, C, Høyland, KV, Granskog, MA. 2022. Drill-hole ridge ice and snow thickness and draft measurements during MOSAiC 2019/20. PANGAEA. doi: 10.1594/PANGAEA.950192

Schmithüsen, H. 2021. Continuous meteorological surface measurement during POLARSTERN cruise PS122/2. Alfred Wegener Institute, Helmholtz Centre for Polar and Marine Research, Bremerhaven, PANGAEA. doi: 10.1594/PANGAEA.935222

Schmithüsen, H. 2021. Continuous meteorological surface measurement during POLARSTERN cruise PS122/3. Alfred Wegener Institute, Helmholtz Centre for Polar and Marine Research, Bremerhaven, PANGAEA. doi: 10.1594/PANGAEA.935223

Schmithüsen, H. 2021. Continuous meteorological surface measurement during POLARSTERN cruise PS122/4. Alfred Wegener Institute, Helmholtz Centre for Polar and Marine Research, Bremerhaven, PANGAEA. doi: 10.1594/PANGAEA.935224

Acknowledgments

This work was carried out and data used in this manuscript were produced as part of the international Multidisciplinary drifting Observatory for the Study of the Arctic Climate (MOSAiC) with the tag MOSAiC20192020 (AWI_PS122_00). We thank all those who contributed to MOSAiC and made this endeavor possible (Nixdorf et al., 2021). We acknowledge especially the assistance from Egor Shimanchuk, Ian Raphael and Juarez Viegas for drilling of the ridges.

Funding

Data used in this manuscript were produced as part of the international MOSAiC project with the tag MOSAiC20192020, Project ID: AWI_PS122_00. BAL, DD, ES, KH, and MAG were supported by the Research Council of Norway through project HAVOC (grant no 280292). BAL and MAG were also supported by Research Council of Norway project CAATEX (grant no 280531) and MAG by the Norwegian Polar Institute. MAG received funding from the European Union's Horizon 2020 research and innovation programme under grant agreement No 101003826 via project CRiceS (Climate Relevant interactions and feedbacks: the key role of sea ice and Snow in the polar and global climate system). CK received funding through the IceScan project (03F0916A) funded by the German Federal Ministry of Education and Research (BMBF). NN was funded through the IceSense (03F0866A) project funded by the German Federal Ministry of Education and Research (BMBF). PI was supported by Research Council of Norway project SIDRiFT (grant no 287871). The European Union's Horizon 2020 research and innovation program projects ARICE (grant no 730965) for berth fees associated with the participation of the DEARice team.

Competing interests

The authors declare that they have no conflict of interest.

Author contributions

Contributed to conception and design: MAG, KVH

Contributed to acquisition of data: ES, DD, BAL, PI, MH, CK

Contributed to analysis and interpretation of data: All authors

Drafted and/or revised the article: ES, MAG, KVH drafted the first version of the manuscript, and all authors contributed to the writing and revisions.

Approved the submitted version for publication: All authors

Supplemental material

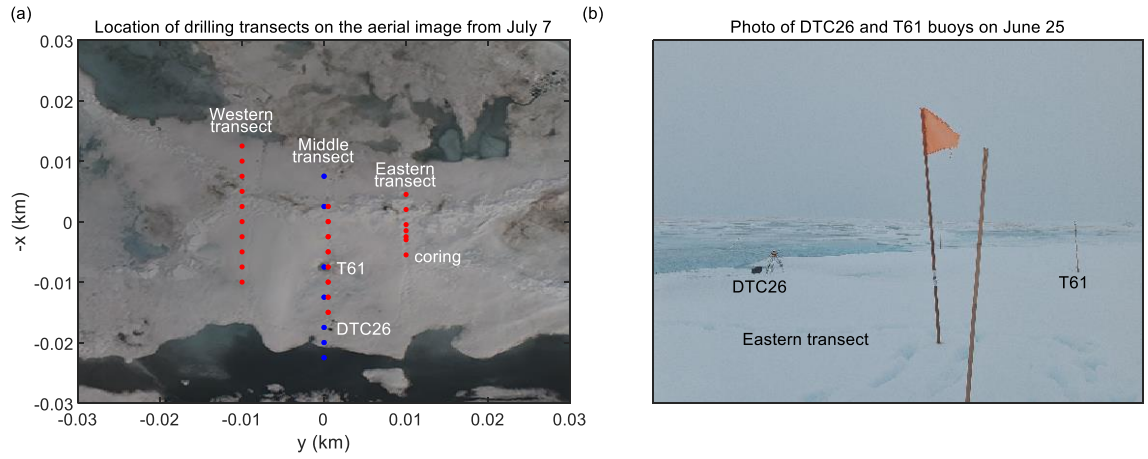

Figure S1. Location of drilling transects at Alli's Ridge. (a) Location of ice mass balance buoys T61 and DTC26, ice drilling transects and ice coring with the background of the aerial image of the ice floe from July 7, and (b) DTC26 and T61 buoys on 25 June (b).

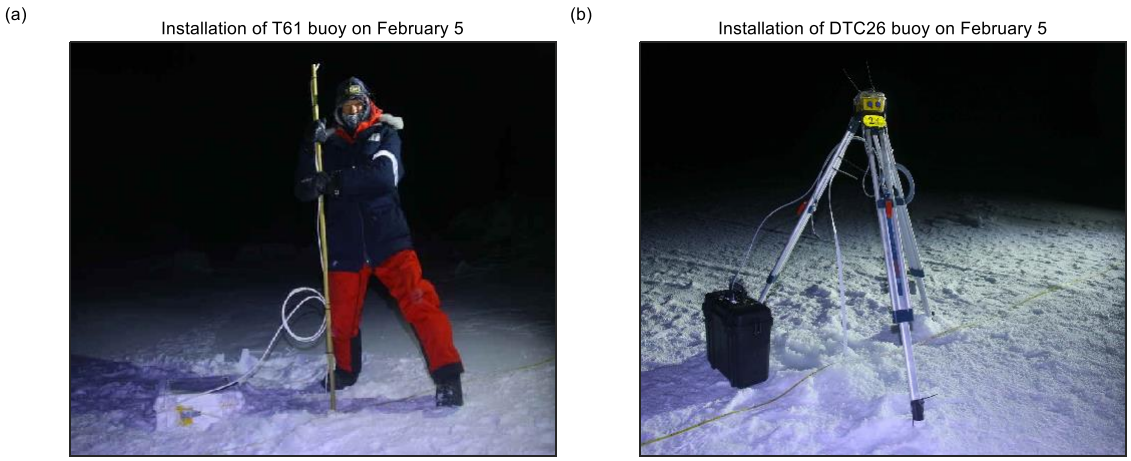

Figure S2. IMB sites. Photos of (a) the T61 and (b) DTC26 buoys during their installation on February 5.

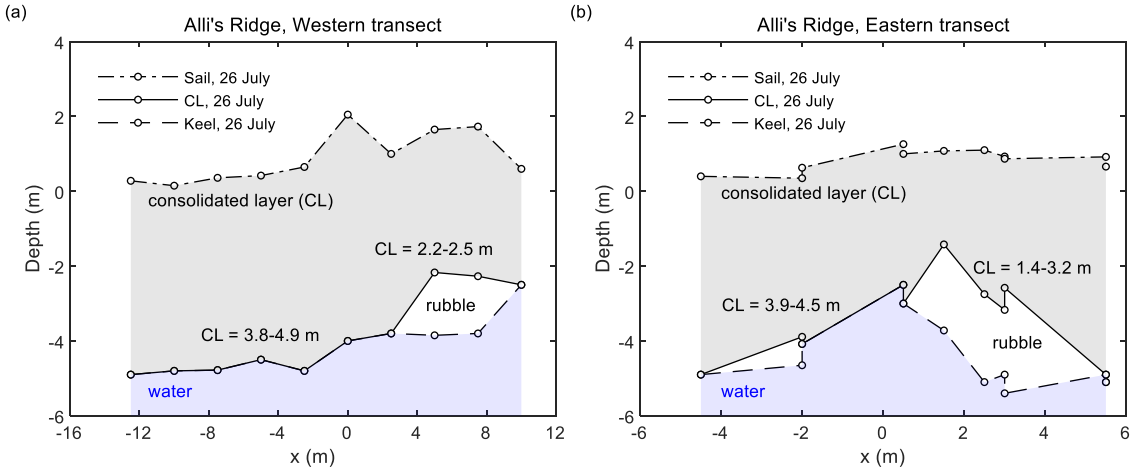

Figure S3. Alli's Ridge morphology for (a) Western and (b) Eastern transect. Depth of sail, consolidated layer, and ridge keel for summer season along a section across the Alli's Ridge for the Western and Eastern transect.